DISSOLUTION OF OXYGEN REDUCTION ELECTROCATALYSTS IN ACIDIC ENVIRONMENT

A Dissertation

by

ZHIHUI GU

Submitted to the Office of Graduate Studies of
Texas A&M University
in partial fulfillment of the requirements for the degree of

DOCTOR OF PHILOSOPHY

December 2007

Major Subject: Chemical Engineering

DISSOLUTION OF OXYGEN REDUCTION ELECTROCATALYSTS IN ACIDIC ENVIRONMENT

A Dissertation

by

ZHIHUI GU

Submitted to the Office of Graduate Studies of
Texas A&M University
in partial fulfillment of the requirements for the degree of

DOCTOR OF PHILOSOPHY

Approved by:

Chair of Committee, Perla B. Balbuena
Committee members, Jorge M. Seminario
Victor M. Ugaz
Manuel P. Soriaga
Head of Department, Michael V. Pishko

December 2007

Major Subject: Chemical Engineering

ABSTRACT

Dissolution of Oxygen Reduction Electrocatalysts in Acidic Environment.

(December 2007)

Zhihui Gu, B.S., Tianjin University

Chair of Advisory Committee: Dr. Perla B. Balbuena

Platinum (Pt) alloy nanoparticles are used as catalysts in electrochemical cells to reduce oxygen to water and to oxidize hydrogen; the overall reaction converts chemical energy into electrical energy. These nanocatalysts are deposited on a carbon substrate and their catalytic function takes place in acid medium. This harsh environment causes an undesired reaction, which is the dissolution of the metal atoms into the acid medium; thus affecting the catalyst life. This dissertation aims to investigate the dissolution mechanism of fuel cell cathode catalysts at the atomic level starting from the oxygen reaction intermediates on the cathode catalyst surface and propose guidelines to improve cathode catalysts durability based on our proposed mechanism. Density functional theory is employed to study various possible scenarios with the goals of understanding the mechanism of the metal atom dissolution process and establishing some guidelines that permit a rational design of catalysts with better stability against dissolution. A thermodynamic analysis of potential metal dissolution reactions in acid medium is presented first, using density functional theory calculations to explore the relative stabilities of transition metals in relation to that of Pt. The study is performed by comparing the change in reaction Gibbs free energies for different metals in a given dissolution reaction. Then, a series of density functional theory studies, tending to investigate the adsorbed atomic oxygen absorption process from cathode catalyst surface into its subsurface, includes: 1) the oxygen adsorption on various catalyst surfaces and oxygen absorption in subsurface sites to figure out the minimum energy pathway and energy barrier of on-surface oxygen migration and absorption into subsurface; 2) the

oxygen coverage, the other oxygen reduction reaction intermediates, and water effects on the oxygen absorption process according to reaction pathways, energy barriers, and thermodynamic analysis; 3) the oxygen absorption process on several Pt-based alloys with various compositions and components to find out the best alloy to inhibit atomic oxygen absorption including both kinetic and thermodynamic analyses, and the effects of such alloyed species on the inhibition process.

ACKNOWLEDGEMENTS

I would like to thank my advisor, Dr Perla B. Balbuena, for her guidance and support throughout my Ph.D. program, including the course of this research. Thanks to advisory committee members, Dr. Seminario, Dr. Ugaz, Dr. Soriaga, and Dr. Schaak for advice and suggestions to this research.

Thanks also to colleagues in Dr. Balbuena's group for helpful discussions on my research projects. I also extend my gratitude to departmental faculty and staff for making my time at Texas A&M University a great experience.

Finally, thanks to my wife, Liheng Gu, and my parents for their love and encouragement.

TABLE OF CONTENTS

CHAPTER Page

LIST OF FIGURES

FIGURE Page

LIST OF TABLES

TABLE Page

CHAPTER I

INTRODUCTION

Proton exchange membrane fuel cells (PEMFCs) are promising and attractive candidates for a variety of power supplies ranging from portable applications, transportation applications, to large scale stationary power systems due to some advantages such as low operating temperature, high current density, and discontinuous operation[1-4]. The electrolyte in PEMFC is an ion conductive polymer membrane (Nafion® being the most well known and well established membrane)[5], which is impermeable to gases but conducts protons. Each side of the membrane is bonded to catalytic porous electrodes. The best catalyst for both cathode and anode is platinum or platinum-based alloy loaded on carbon black support[6,7] or on newly developed nano-materials such as carbon nanotubes or carbon fibers[8,9]. Carbon-supported platinum or platinum-based alloy catalysts are now commonly used as electrodes in polymer electrolyte membrane fuel cells to catalyze the hydrogen oxidation on the anode and the oxygen reduction reaction (ORR) on the cathode side[10]:

anode: $2H_2 \rightarrow 4H^+ + 4e^-$

cathode: $O_2 + 4e^- + 4H^+ \rightarrow 2H_2O$

overall: $2H_2 + O_2 \rightarrow 2H_2O$.

At the anode, the hydrogen splits into protons and electrons. The protons travel through the proton conductive polymer membrane to the cathode, while the electrons travel through the external circuit to the cathode. At the cathode, oxygen molecules interact with the protons and electrons to generate water. The net result of these simultaneous electrochemical reactions produces direct electrical current through an external circuit. The theoretical potential of the above cathode reaction is 1.23 V at 25^{o}C and atmospheric pressure based on the reaction Gibbs free energy and using the Nernstian equation. The much slower kinetics of the oxygen reduction reaction is one of the key points that needs to be addressed for improving the fuel cell operation efficiency[11]. Therefore, many research studies related to the analysis of the oxygen reduction reaction process catalyzed by platinum and platinum-based alloy surfaces have been reported

---

This dissertation follows the style of The Journal of Physical Chemistry.

experimentally and theoretically[12-20]. In those studies the oxygen adsorption and dissociation process has been proposed as a series of proton and electron transfer reactions, and the existence of oxygenated intermediates such as adsorbed O, OH, and OOH on the cathode catalyst surface during the oxygen reduction reaction process have been established. The stable active surfaces of the platinum cathode in acidic electrolyte environment for oxygen reduction reaction are the (111), (100), and (110) [21-23]. Platinum-based alloys have shown similar catalyzing activity to pure platinum catalyst for the oxygen reduction reaction[24-26], and in some cases higher activities of Platinum-based alloys than pure platinum were suggested by experimental reports[27-29] in which Co, Ni, Cr, Fe as the second metal species are commonly employed in Pt-based bimetallic cathode catalysts. The enhanced oxygen reduction reaction activity could be due to one or more of following effects: modification of the electronic structure of platinum (valence d orbital vacancies); physical structure of platinum change such as shorter Pt bond distance; adsorption of oxygen onto alloying elements.

The challenge for the long term application is the durability of PEMFC under the operational conditions. The polymer electrolyte membrane durability, gas diffusion layer durability, and electrode catalyst durability are the major barriers to commercialization of PEMFC systems for stationary and transportation applications[30-34]. The main properties of polymer electrolyte membrane are proton conductivity, water transport, gas permeation, and physical properties such as strength and dimensional stability. The durability of gas diffusion layer depends on its porosity and hydrophobicity, whereas the cathode catalyst durability mainly depends on active surface loss. Durability of Pt or Pt-based alloy cathode catalysts in acid environment during PEMFC operation is one of the main challenges for long-term applications, as the electrode active surface loss of cathode results in substantial decrease of fuel cell performance[35]. The platinum active surface loss takes place especially in the conditions of high electrode potentials[36-38] and under fuel starvation[39,40]. Loss of platinum can occur due to corrosion of carbon black support or oxidation of platinum[41]. Platinum loss caused by carbon support corrosion was observed through the decrease of cathode thickness and appearance of non-

supported platinum particles after PEMFC operation[41]. It was also reported that agglomeration of active platinum nanoparticles caused by dissolution of the smallest particles or active sites and subsequent sintering are one of the major reasons for the loss of active surface in phosphoric acid fuel cells[42-44]. For PEMFC, losses of electrocatalyst active surface due to cathode catalyst cluster size distribution increasing were detected during PEMFC operation by comparing the fresh with the aged cathode catalyst through high resolution transmission electron microscopy (HRTEM) images[41]. The presence of Pt and Cr (one of the alloy metals) in the cathode outlet water[45] and Pt cations inside the proton exchange membrane observed by UV detection[41] indicate that the dissolution of the cathode catalyst is another main reason for cathode active surface loss. The dissolved platinum species can redeposit on the Pt particles to form larger particles following an Ostwald ripening process[46,47] and also can diffuse out of the membrane electrode assembly becoming deposited on the polymer membrane[48] concomitant with a decrease in platinum cathode active surface. The precipitation of Pt in the electrolyte membrane close to the cathode and at the catalyst/membrane interface due to reduction of dissolved platinum species such as Pt^{2+} by permeating hydrogen[35,49] and the presence of platinum cation in the PEMFC cathode outlet water indicate that Pt dissolution plays an important role in PEMFC cathode catalyst active surface losses [35]. Simultaneous presence of Pt^{2+} and Pt^{4+} was evidenced in the decantation solution of aged membranes in 1.33 M NaCl solution in the platinum dissolution experiment[41]. The exact nature of the Pt cation complex dissolution out of cathode catalyst is unknown and free Pt cations do not exist in either ionomer phase or in solution. The platinum cations are likely solvated by water molecules and formation of platinum complexes with other ions such as fluoride is also very likely in PEMFC environment. Fluoride and sulfate ions were detected in the PEMFC cathode water outlet and the degradation of membrane was confirmed[45]. The platinum complex form before the dissolution could be also critical for the dissolution process; therefore, the investigation of possible platinum cation complexes could also provide a guidance to prevent cathode catalyst dissolution. Experimental reports on Pt and Pt-alloy cathode catalysts showed that Pd and Rh are more soluble than Pt in the

same experimental conditions[50] and the metal dissolution rate of a Pt alloy with PtM ratio of 3:1 is lower than that of a Pt alloy with PtM ratio of 1:1 (M= Co, Ni)[49]. Improved durability of PtCo/C in PEMFC operation was also reported by comparing with pure platinum[51]. In this dissertation we focus on the stability of cathode catalysts and on the elucidation of the corresponding cathode catalyst dissolution mechanism exploration.

Platinum dissolution in PEMFC depends on factors such as temperature[52], electrode potential[52-54], and presence of oxide formation[55,56]. The Pourbaix diagram shows that platinum is unstable at a potential range of 1.0 ~ 1.2 V versus SHE at pH values less than or equal to 1.0. Dissolution based on the weight change of the cathode was not observed at operational temperatures lower than 40°C in 1 M $HClO_4$ electrolyte even at high potential of 1.2 V versus SHE and the dissolution rate at 80°C is much higher than at 60°C through the potential range from 0.95 V to 1.15 V under potentiostatic conditions[52], indicating that dissolution is highly dependent on temperature. A mathematical model was developed for platinum cathode dissolution in PEMFCs, which considered both the potential dependence dissolution of platinum and the chemical dissolution of platinum oxide[55,56]. It was reported that the equilibrium concentration of dissolved platinum in perchloric acid electrolyte increased monotonically under potentiostatic conditions for potentials larger than 0.6 V versus standard hydrogen electrode (SHE) but decreased for potentials greater than 1.1 V vs. SHE[57]. The dissolution of platinum could be activated by potential, and higher potential should cause higher electronic oxidation of platinum and corresponding higher dissolution concentration. Therefore, it appears interesting to explore the detailed dissolution mechanism and to relate to the oxide formation on the platinum cathode. In the range of potentials from 0.85 to 1.15 V, half monolayer of oxygen atoms is adsorbed on the cathode catalyst[58,59] and from 1.15 to 1.2 V, a second half oxygen atom monolayer is formed on the catalyst surface and it is suggested that a place exchange of adsorbed oxygen atoms with the surface platinum atoms takes place with further formation of an adsorbed oxygen layer[58,60]. This place exchange would make the oxygen atoms to

diffuse into the subsurface leaving the platinum atoms exposed to the electrolyte for further oxidation and dissolution. It has been reported that atomic oxygen can be found in the subsurface of transition metals such as Pt, Pd, and Ru during surface reactions in various experimental environments[61-66] and that subsurface oxygen can affect the reactivity of a catalytic surface[67-69]; for example, subsurface oxygen increased the kinetics of H_2, O_2, and NO dissociation on Ag(111) surface. Subsurface oxygen may be further considered as the initial stage in the corrosion and growth of metal oxides[70]. Under electrochemical conditions subsurface oxygen can be formed in the oxidation of polycrystalline platinum and the concentration of subsurface oxygen has been found to depend on the cycling rate by cyclic voltammetry experiments[71,72]. Possible structures of the initial stages of the oxidized surface have been also proposed in which the oxygen atom migrates into subsurface by place exchange between Pt atom and atomic oxygen[73,74] to form platinum oxide. However, the microscopic understanding of this complex process is at its infancy. It is important to remark that the initial stages of formation of surface oxide correlate with Pt dissolution, and both oxygen coverage and Pt dissolution are functions of potential [48]. Moreover, many other studies have also linked the initial step of surface oxide formation with the initial corrosion stages[70]. On the other hand, single crystal studies of gas-phase adsorption of oxygenated compounds have proven to be fundamental[75-77] not only to understand oxygen reactivity but also to guide the design of Pt-alloy electrocatalysts to improve activity. By analogy, it is expected that fundamental studies of incorporation of oxygen into the subsurface of relevant crystallographic facets will be also important to elucidate the initial stages of oxide growth and their relationship with the metal corrosion process. In this dissertation we present a series of studies tending to investigate the subsurface oxygen formation process and correlate our observations to the experimental cathode dissolution process. Stable structures of electrode metal catalysts in acidic environment are the (111), (100), (110) surfaces[21-23] and the oxygen reduction reaction can take place on those (h k l) surfaces though its kinetics vary with the crystal facet depending on the electrolyte[78]. Our calculations are done on Pt(100) and Pt(111) surfaces. We characterize the site

preference of an oxygen atom adsorbed on Pt(111) and Pt(100) surfaces as a function of coverage, the absorption of atomic oxygen inside Pt(111) and Pt(100) subsurfaces, and the migration of an oxygen atom from low surface coverage into the subsurface.

In contrast to the extensive and detailed investigations reported about the oxygen reduction reaction process on PEMFC catalytic cathode surfaces, the knowledge on the detailed cathode dissolution process remains limited at atomic level and a detailed analysis of the mechanisms behind the dissolution process of cathode catalysts has not been reported. This dissertation aims to investigate the dissolution mechanism of fuel cell cathode catalysts at the atomic level starting from the oxygen reaction intermediates on the cathode catalyst surface and propose guidelines to improve cathode catalysts durability based on our proposed mechanism. In this dissertation, a thermodynamic analysis of potential metal dissolution reactions in acid medium is presented first, using density functional theory (DFT) calculations to explore the relative stabilities of transition metals in relation to that of Pt. The study is performed by comparing the change in reaction Gibbs free energies for different metals in a given dissolution reaction. Then, a series of studies, tending to investigate the adsorbed atomic oxygen absorption process from cathode catalyst surface into its subsurface by DFT calculations, includes: 1) the oxygen adsorption on various catalyst surfaces and oxygen absorption in subsurface sites to figure out the minimum energy pathway and energy barrier of on-surface oxygen migration and absorption into subsurface; 2) the oxygen coverage, the other oxygen reduction reaction intermediates, and water effects on the oxygen absorption process according to reaction pathways, energy barriers, and thermodynamic analysis; 3) the oxygen absorption process on several Pt-based alloys with various compositions and components to find out the best alloy to inhibit atomic oxygen absorption including both kinetic and thermodynamic analyses, and the effects of such alloyed species on the inhibition process.

CHAPTER II

METHODOLOGIES

Density functional theory (DFT) was used for all of calculations in this report. The ground-state energy, wave function, and all other molecular electronic properties of a many body system are uniquely determined by the ground state electron probability density, a function of only three variables according to Hohenberg-Kohn Theorem[79]. The ground-state electronic wave function of an n-electron molecule is an eigenfunction of the purely electronic Hamiltonian operator:

$$\mathrm{H} = -\frac{1}{2}\sum_{i=1}^{n}\nabla_i^2 + \sum_{i}^{n} v(r_i) + \sum_{j}\sum_{i>j}\frac{1}{r_{ij}},\ v(r_i) = -\sum_{\alpha}\frac{Z_\alpha}{R_{i\alpha}}$$

The $v(r_i)$ is called external potential acting on electron *i* in DFT. The corresponding total energy functional is following:

$$E_0 = E_v(\rho_0) = \langle T(\rho_0)\rangle + \langle V_{Ne}(\rho_0)\rangle + \langle V_{ee}(\rho_0)\rangle$$

Here T, V_{Ne}, and V_{ee} denote kinetic energy, external potential, and electron repulsion term respectively. Because the kinetic and repulsion energy functionals are unknown, the Hohenberg-Kohn Theorem did not provide a practical way to calculate E_0. The Kohn-Sham Self-consistent Field Methodology devised a practical method to find electron density and find energy from the corresponding electron density distribution, though the equations of Kohn-Sham method contain unknown exchange and correlation functional which must be reasonably approximated[80]. A fictitious reference system (called non-interacting system, denote by subscript s) of n non-interacting electrons was considered. Therefore the total energy functional can be rewritten as following:

$$E(\rho) = \langle T^s(\rho)\rangle + \langle V_{Ne}(\rho)\rangle + \langle V_{ee}{}^s(\rho)\rangle + E^{xc}(\rho),\ E^{xc}(\rho) = \Delta\langle T(\rho)\rangle + \Delta\langle V_{ee}(\rho)\rangle$$

$$\Delta\langle T(\rho)\rangle = \langle T(\rho)\rangle - \langle T^s(\rho)\rangle;\ \Delta\langle V_{ee}(\rho)\rangle = \langle V_{ee}(\rho)\rangle - \langle V_{ee}{}^s(\rho)\rangle$$

E^{xc} is called exchange and correlation functional which includes terms accounting for both exchange energy and the electron correlation, which is omitted from Hartree-Fock theory. Now the only unknown term is E^{xc} functional and the key to accurate Kohn-

Sham DFT calculation of molecular properties is to obtain a good approximation to the exchange and correlation functional. There are types of exchange and correlation functionals which have been developed such as local density approximation (LDA), generalized-gradient approximation (GGA) and hybrid exchange-correlation functionals. The commonly used exchange functionals are Perdew-Wang's 1991 functional (PW91)[81-83] and Becke's 1988 functional (B)[84] and commonly used correlation functionals are Lee-Yang-Parr (LYP)[85], Perdew-Wang's PW91[81-83], Perdew's P86[86], and Becke's B95[87]. The hybrid exchange-correlation functionals are widely used such as B3LYP and B3PW91[88,89]. The Perdew-Burke-Ernzerhof (PBE)[90,91] exchange-correlation functional is also widely used. The wave function is constructed by the basis set which is a set of mathematical functions and each molecular orbital can be expressed as a linear combination of basis functions, the coefficients for which are determined from the iterative solution of Self-consistent Field Kohn-Sham equation. The pseudopotential is an attempt to replace the complicated effects of the motion of the core (non-valence) electrons of an atom or ion and its nucleus potential with an effective pseudopotential, because most physical properties of solids are dependent on the valence electrons much greater than that of the tightly bound core electrons. By construction of a pseudopotential, the valence wavefunction generated is also guaranteed to be orthogonal to all the core states. Various types of basis sets and pseudopotentials are applied in Kohn-Sham DFT calculation in various codes and final step is the solution the Kohn-Sham equation.

In chapter III the Gaussian03 Rev C.02 program package[92] was employed for all calculations. All geometries were fully optimized using B3LYP, which is the hybrid exchange functional Becke3[93] in combination with the LYP correlation functional[85], with the LANL2DZ pseudopotential and double ξ basis set for transition metals[94] and with 6-311++g(d, p) for oxygen and hydrogen atoms. Frequency calculations were done for all optimized geometries at the same theoretical level as that of the geometry optimization to verify that the structures were global minima and to calculate the free energies. Different geometric, electronic and spin states were calculated for all species

and only the ground states were used to calculate the free energy difference for the metal dissolution reactions. Slab and small clusters usually are used to model metal surfaces for studying oxygen adsorption and reduction reactions using DFT calculations, providing reasonable results[17,77,95-98]. For the cathode catalyst dissolution process, our investigation starts analyzing the oxygen reduction intermediates adsorbed on a metal M (MO, MOH, MOOH), where M is represented by a single atom or by a dimer. Comparison of the ΔG for each possible dissolution reaction provides the thermodynamic relative stabilities of metal catalysts against dissolution, though the single atom and the dimer models are approximations to the catalytic site. We focus on the free energy differences of metal dissolution reactions which could cancel the errors arising from the approximate metal model to some extent and can provide valuable predictions.

In chapter IV to chapter VI we investigated the adsorbed on-surface atomic oxygen absorption into subsurface process. All calculations were performed by using spin polarized density functional theory in the generalized gradient approximation and the PBE functional[91] for electron exchange and correlation. The Vienna Ab Initio Simulation Package (VASP) [99,100] was used to solve the Kohn-Sham equations in a simulation cell with periodic boundary conditions using plane wave basis sets in which the Blöch's all electron projector augmented (PAW) method[101]with frozen core approximation is implemented[102]. Energy cutoff of 400 eV is used for all calculations and the convergence criterion for structure relaxation is that the force acting on each atom becomes less than 0.01eV/Å. The Monkhorst-Pack scheme[103] was employed for the k-point sampling and the calculated bulk equilibrium lattice constant of fcc Pt and fcc Pt-based alloys. The calculated lattice constant of fcc Pt is 3.977 Å with the converged k-mesh of 14×14×14, which agrees within 1.45% with the experimental value of 3.92[104] and the calculated lattice constants of various Pt-based alloys with same k-mesh of 14×14×14 are listed in chapter VI, which agree well with experimental data. The Pt(100) and Pt(111) surfaces are modeled in the supercell approach using a five layer Pt or Pt-based alloy slabs in which the three top layers are allowed to relax and the

two bottom layers are fixed at the calculated bulk positions. A vacuum space is approximately equal to 12 Å above the top layer in both Pt(100) and Pt(111) surface cases. For oxygen adsorption on surface and absorption into subsurface, we investigated coverages of 1ML (one monolayer, defined as one oxygen atom per each surface atom), 0.5 ML, 0.25 ML, and 0.11 ML on Pt(100) and Pt(111) surfaces. For absorption into the subsurfaces, we investigated 0.11, 0.25, 0.50 ML subsurface coverages at various surface coverages. Monkhorst-Pack grids of 14×14×1, 11×11×1, 5×5×1, 3×3×1 were used for corresponding Pt(100) (1×1),√2×√2, (2×2), (3×3) cells, and for Pt(111) (1×1), (2×1), (2×2), (3×3) cells respectively. The stabilities of oxygen adsorption on different sites, such as top, bridge, and hollow sites were investigated according to their corresponding binding energies, and the stabilities of oxygen absorption in the subsurface sites, inside tetrahedral or octahedral sites, were evaluated according to their corresponding absorption energies. The binding energies of oxygen adsorption on Pt surfaces and absorption energy in subsurfaces are defined in equation: $E = E_{Pt_nO} - E_{Pt_n} - E_O$. E_{Pt_nO} is the energy of oxygen adsorption on Pt surface or energy of oxygen absorption in Pt subsurface, and n stands for the number of Pt atoms in the different cells. E_{Pt_n} is the energy of clean Pt surfaces and E_O is the energy of an isolated oxygen atom at its ground state. E_{Pt_nO} and E_{Pt_n} were calculated with the above mentioned calculation methods and corresponding k-meshes and E_O was calculated with a single oxygen atom in a cubic unit cell with 8 Å in each dimension. The climbing image nudged elastic band method (cNEB)[105-107] was employed to investigate the saddle points and minimum energy paths (MEP) for oxygen adsorption on Pt surfaces and diffusion into Pt subsurfaces in both Pt(100) and Pt(111) cases. In this report the (2×2) and (3×3) cells corresponding to 0.25 ML and 0.11 ML coverage were used to study the minimum energy paths, transition states and corresponding energy barriers of oxygen absorption into the subsurfaces.

It should be marked here that the models of dissolution, adsorption, and absorption systems in this study are not the real conditions under which the cathode catalyst of PEMFC operation. The surface structure and composition of cathode catalyst could be

very different from our models and the chemical properties of cathode could be influenced by external field and chemical environment. However, single crystal studies of gas-phase adsorption of oxygenated compounds have proven to be fundamental[75-77] not only to understand oxygen reactivity but also to guide the design of Pt-alloy electrocatalysts. By analogy, it is expected that fundamental studies of incorporation of oxygen into the subsurface of relevant crystallographic facets will be also important to elucidate the initial stages of oxide growth and their relationship with the metal corrosion process.

CHAPTER III

THERMODYNAMIC ANALYSIS OF RELATIVE STABILITIES OF VARIOUS TRANSITION METALS IN CATHODE CATALYSTS

In this chapter the reaction thermodynamics of a group of chemical and electrochemical reactions were chosen to investigate the dissolution of metal atoms from oxygen reduction reaction catalysts in an acid medium. Once a set of thermodynamically allowed reactions is established, those reactions are selected to investigate the relative stabilities of Pt atoms and of other transition metal atoms towards the dissolution reactions. Six transition metal atoms M (Co, Rh, Ir, Ni, Pd, Pt) from group VIIIA are used to model adsorption sites of oxygen reduction intermediates denoted as MO, MOH and MOOH. Proposed dissolution reactions are listed in Scheme 3.1.

Reaction 1: $MOOH + 3H^+ + e^- \longrightarrow M^{2+} + 2H_2O$

Reaction 2: $MOH + MO + 3H^+ + e^- \longrightarrow M^{2+} + M + 2H_2O$

Reaction 3: $MOOH + MO + 5H^+ + e^- \longrightarrow 2M^{2+} + 3H_2O$

Reaction 4: $MOOH + MO + 5H^+ + 3e^- \longrightarrow M^{2+} + M + 3H_2O$

Reaction 5: $MOOH + MOH + 4H^+ + 2e^- \longrightarrow M^{2+} + M + 3H_2O$

Reaction 6: $MO + 2H^+ \longrightarrow M^{2+} + H_2O$

Reaction 7: $2MOH + 2H^+ \longrightarrow M^{2+} + M + 2H_2O$

Reaction 8: $MOOH + MOH + 4H^+ \longrightarrow 2M^{2+} + 3H_2O$

Scheme 3.1. Possible metal dissolution reactions

The solvated proton is modeled as $H_9O_4^+$ (four waters in the first hydration shell[108]) and the hydrated metal cations (M^{2+}) are modeled as $M(H_2O)_4^{2+}$ and $M(H_2O)_6^{2+}$ because divalent states and four-coordinate and six-coordinate complexes of transition metals are common[109]. In each electrochemical reaction, the electron energy is set to zero. Slab and small clusters usually are used to model metal surfaces for studying oxygen adsorption and reduction reactions using DFT calculations, providing reasonable results[17,77,95-98]. For the cathode catalyst dissolution process, our investigation starts analyzing the oxygen reduction intermediates adsorbed on a metal M (MO, MOH, MOOH), where M

is represented by a single atom or by a dimer. Comparison of the ΔG for each possible dissolution reaction provides the thermodynamic relative stabilities of metal catalysts against dissolution, though the single atom and the dimer models are approximations to the catalytic site. We focus on the free energy differences of metal dissolution reactions which could cancel the errors arising from the approximate metal model to some extent and can provide valuable predictions. The ΔG for each dissolution reaction is calculated as the difference between products and reactants, for example, reaction 2 in Scheme 1 for a single metal atom M and for a metal dimer MM model with the hydrated metal cation modeled as $M(H_2O)_6^{2+}$ are written as (1) and (2) respectively:

$$\Delta G = G_{M(H_2O)_6^{2+}} + G_M + 3G_{(H_2O)_4} + 2G_{H_2O} - G_{MOH} - G_{MO} - 3G_{H_9O_4^+} - G_{(H_2O)_6} \quad (1)$$

$$\Delta G = G_{M(H_2O)_6^{2+}} + G_M + G_{MM} + 3G_{(H_2O)_4} + 2G_{H_2O} - G_{MMOH} - G_{MMO} - 3G_{H_9O_4^+} - G_{(H_2O)_6} \quad (2)$$

3.1. Thermodynamic Analysis of Pt Dissolution. The possible metal dissolution reactions from oxygen reduction intermediates of MO, MOH and MOOH proposed in Scheme 3.1 include both chemical and electrochemical dissolution reactions. In reactions of 1, 6, and 7, the oxygen reduction intermediates interact with a proton to produce metal cations, and in reactions of 2 to 5 and in reaction 8 adjacent oxygen reduction intermediates adsorbed on the catalyst surface interact with each other and with a proton to produce metal cations and water. The calculated Gibbs free energy changes of reaction 1 to reaction 8 are listed in Table 3.1. The difference between the ΔG of a given dissolution reaction in Table 3.1 is due to the variation in the hydration energies of the cation with different water coordination number, and to the metal bond dissociation energy involved in the dimer model. The ΔGs of reactions 6, 7, and 8 are positive whereas the ΔGs of the other reactions are negative (except Pt dimer in R. 3 in $Pt(H_2O)_4^{2+}$ model), indicating that all of the dissolution reactions are thermodynamically favorable except for reactions 6, 7, and 8 with $Pt(H_2O)_6^{2+}$ model. From Scheme 3.1, the thermodynamic favorable dissolution reactions are electrochemical, whereas, the chemical dissolution reactions 6, 7, and 8 are thermodynamically unfavorable. Among the thermodynamic favorable dissolution reactions, reaction 4 has the highest negative

Δ G, which indicates that the more electrons involved, the higher the equilibrium constant of the associated reaction. The conclusions arising from this initial set of calculations are that the possible Pt cathode catalyst dissolution reactions (1 to 5 in Scheme 1) are electrochemical, and that all the oxygen reduction intermediates can be involved in the dissolution reactions. The elementary reactions and corresponding mechanism for each thermodynamically favorable dissolution reaction should be further investigated to detail the dissolution mechanism.

Table 3.1: Gibbs free energies (Δ G, in eV) of possible Pt dissolution reactions (in Scheme 1). Δ Gs are calculated with B3LYP/Lan2dz & 6-311++g(d,p), modeling the hydrated cation as $Pt^{2+}(H_2O)_4$ and as $Pt^{2+}(H_2O)_6$.

Reactions	ΔG^a	ΔG^b	ΔG^c	ΔG^d
1	-6.26	-7.12	-4.14	-5.00
2	-4.02	-4.88	-2.82	-3.68
3	-3.54	-5.25	0.05	-1.66
4	-20.59	-21.44	-19.32	-20.17
5	-13.01	-13.87	-11.18	-12.04
6	2.72	1.88	4.20	3.34
7	3.55	2.69	5.30	4.45
8	4.04	2.32	5.87	4.16

[a]. Pt^{2+} modeled as $Pt^{2+}(H_2O)_4$ and single metal atom model;
[b]. Pt^{2+} modeled as $Pt^{2+}(H_2O)_6$ and single metal atom model;
[c]. Pt^{2+} modeled as $Pt^{2+}(H_2O)_4$ and metal dimer model;
[d]. Pt^{2+} modeled as $Pt^{2+}(H_2O)_6$ and metal dimer model.

3.2. Thermodynamic Analysis of the Stability against Dissolution of Metals Other Than Pt. During the cathode catalyst dissolution process, metal-metal bond dissociation processes are involved which are followed by cation hydration. Therefore,

at least two metal atoms should be included in the cathode catalyst model. However, initially we compute the single metal atom relative dissolution stability as the simplest catalyst model, and we compare the results with those of a dimer model of dissolution. Other five metals (Co, Rh, Ir, Ni, Pd) besides Pt were studied based on the five thermodynamically favorable dissolution reactions. The calculated ΔGs for these metals (using single atom and metal dimer models) for dissolution reactions 1 to 5 (Scheme 3.1) are negative (except some dimer cases in Reaction 3; data available in appendix A) based on $M(H_2O)_4^{2+}$ and $M(H_2O)_6^{2+}$ respectively, which indicates that the dissolution reactions for almost all these metals are also thermodynamically favorable. The ΔG of reaction 4 in which the highest number of electrons are involved has the highest negative value for all the studied metals. Figure 3.1a shows the relative stability of each of the metal atoms relative to Pt for each dissolution reaction based on $\Delta\Delta$G which is defined as:

$\Delta\Delta G = \Delta G_M - \Delta G_{Pt,}$ M = Ir, Pd, Rh, Ni, Co

Negative $\Delta\Delta$G means that the corresponding metal is more unstable than the Pt atom in the given dissolution reaction in acid medium. For each reaction, Co and Ni are the metals which are more easily dissolved than other four metals from the point of view of thermodynamics, with ΔGs significantly more negative (> 2.0 eV) than that of the Pt atom, especially in reaction 3, whereas, Pt and Ir are the most stable metals according to this criterion (Figure 3.1a). The stability of Ir is very similar to Pt in all reactions except in reaction 4, in which Ir is more stable with a $\Delta\Delta$G value of ~ 0.8 eV. Generally Pd is more unstable compared with the Pt atom and the range of variation of $\Delta\Delta$G for the five dissolution reactions in this case is 0.2 to -1.4 eV. Rh is also more unstable compared with Pt and the $\Delta\Delta$G values converge around -0.7 eV except for reaction 3. In summary, using the single atom model, the dissolution stability sequence is Co < Rh < Ir in the ninth column and Ni < Pd < Pt in the tenth column (group VIIIA) of the periodic table.

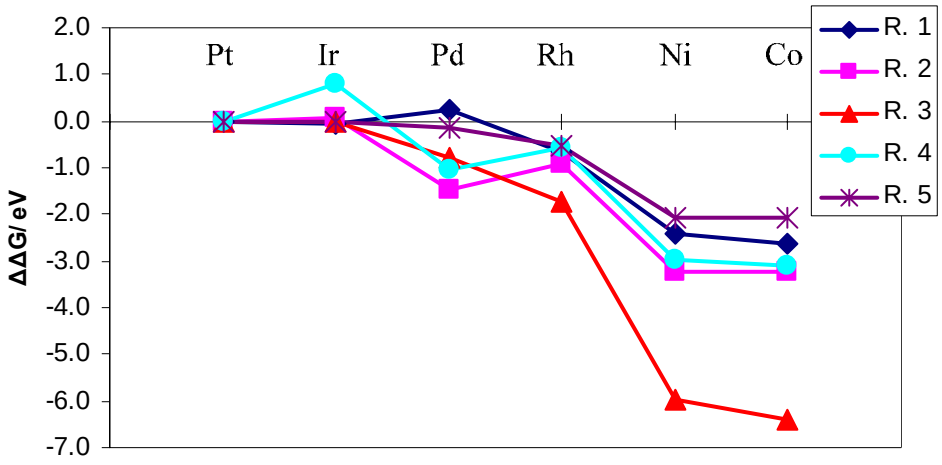

(a)

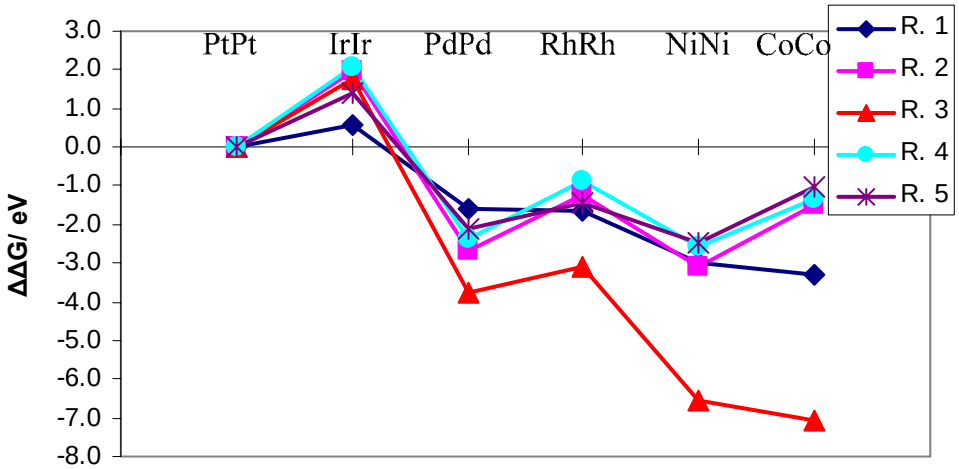

(b)

Figure 3.1. Δ Δ G (eV) of possible dissolution reactions of Pt, Pd, Ni, Ir, Rh, Co. **(a)** single atom model based on $M(H_2O)_6^{2+}$ calculated with B3LYP/LANL2DZ and 6-311++g(d,p). **(b)** dimer model based on $M(H_2O)_6^{2+}$ with B3LYP/LANL2DZ and 6-311++g(d,p).

Figure 3.1b shows the relative stabilities of metal catalysts based on the dimer catalyst model in which the metal bond dissociation is included, and consequently, we expect the results to be more realistic than those of the single atom catalyst model.

Different from the single atom model, Ir is more stable than Pt catalyst with positive $\Delta\Delta G$s for all dissolution reactions, due to the higher dissociation energy of 2.85 eV of the Ir dimer compared to 2.32 eV dissociation energy of the Pt dimer. Similarly to the single atom model results, Pd and Rh are more unstable than Pt for the electrochemical dissolution reactions. In contrast to the single atom model, Rh shows slightly improved stability than Pd in all five dissolution reactions. In the single atom model, Co and Ni have similar stabilities relative to Pt (Figure 3.1a), whereas, Figure 3.1b shows that the Co catalyst is more stable than the Ni cathode catalyst in most of the dissolution reactions including the metal bond dissociation. Figure 3.1b also shows that the Ni catalyst is the most unstable among the six types of metal cathode catalysts. In summary, since the stability of the cathode catalysts against dissolution depends on the combined effects of all dissolution reactions, an approximate relative stability order from Figure 3.1b is Ir > Pt > Rh > Pd > Co > Ni based on the average values of $\Delta\Delta G$ (1.55 eV, 0 ,-1.65 eV, -2.50 eV, -2.85 eV, -3.53 eV respectively).

3.3. Pt Stability against Dissolution in Pt-based Bimetallic Alloy Cathode Catalysts. Pt-M alloys were studied based on the thermodynamically stable five dissolution reactions (Scheme 3.1) to investigate the effects of the introduction of a second metal on the Pt stability against dissolution compared with that of pure Pt. Alloy cathode catalysts with Pt:M ratio of 1: 1 are modeled as Pt-M dimer and the O, OH, and OOH adsorbents assumed to bind to Pt sites. Figure 3.2 shows the relative Pt site stabilities of five types of cathode alloy catalysts compared with that of pure Pt based on the dissolution reactions for which as $\Delta\Delta G$ is defined as:

$$\Delta\Delta G = \Delta G_{PtM} - \Delta G_{PtPt,}\ M = Ir, Pd, Rh, Ni, Co$$

Negative $\Delta\Delta G$ means that Pt in the corresponding alloy is more unstable than pure Pt for a given dissolution reaction in acid medium. Figure 3.2 shows that pure Pt is most stable than Pt in other five alloy catalysts and the presence of a second metal species decreases the stability of Pt adsorption sites. Introduction of Ir, Pd, and Rh decreases the Pt stability in alloy catalysts of PtIr, PtPd and PtRh more than that it does Ni in PtNi. Pt in PtNi almost has similar stability to the pure Pt cathode catalyst, whereas, Pt in PtCo

alloy is the most unstable cathode catalyst of this group. Our calculation results showing that the 1:1 PtNi alloy cathode catalyst is more stable than the 1:1 PtCo alloy cathode are consistent with the experimental report in which PtNi/C cathode alloy catalysts showed lower dissolution rate than PtCo/C alloy catalysts[49]. From Figure 3.2, Ni is the best metal to be alloyed with the Pt catalyst without decreasing the Pt stability against dissolution; obviously this criterion does not refer to optimizing the catalyst in terms of oxygen reduction activity.

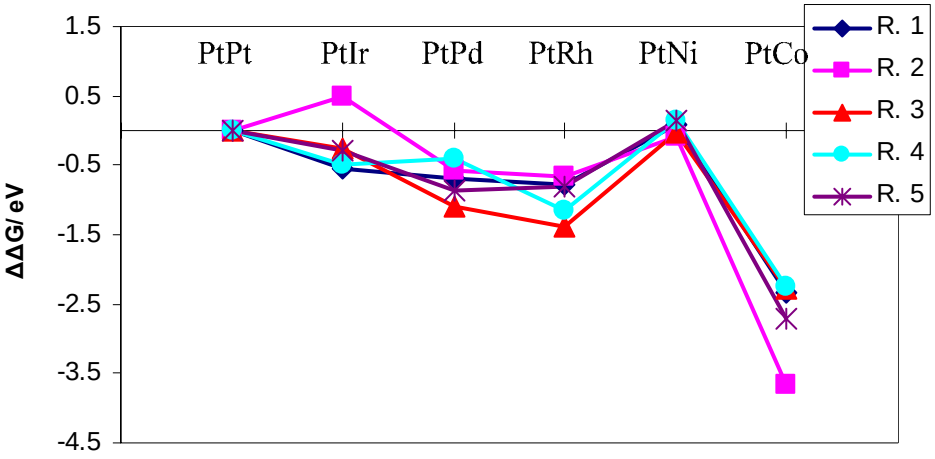

Figure 3.2. $\Delta\,\Delta G$ (eV) of Pt dissolution reactions in Pt alloys. PtPt, PtPd, PtNi, PtIr, PtRh, and PtCo alloy cathode catalysts are calculated based on $M(H_2O)_6^{2+}$ with B3LYP/LANL2DZ and 6-311++g(d,p).

3.4. Alloyed Metal Stability against Dissolution in Pt-based Bimetallic Alloy Cathode Catalysts. In the previous section we discussed the Pt relative stabilities in alloy catalysts compared with that of Pt in a pure Pt cathode catalyst. In an alloy, it is also important to determine the relative stabilities of the second metal M species. Here the adsorption sites are M sites to which the O, OH, and OOH are assumed to bind instead of binding to Pt, with the $\Delta\,\Delta G$ defined as:

$\Delta\,\Delta G = \Delta G_{PtM} - \Delta G_{PtPt,}$ M = Pt, Ir, Pd, Rh, Ni, Co

The values of $\Delta\,\Delta G$ shown in Figure 3.3 indicate that all dissolution reactions show very similar trends of relative dissolution stabilities as those in Figure 3.1b for the respective pure metals. Ni and Co show much lower stability in reaction 3 than other metal species. Ir is the most stable metal in Pt-based bimetallic alloy compared with the other four metals (Pd, Rh, Ni, Co) in PtM alloys and even more stable than Pt in pure Pt cathode catalyst. Approximately, Pd, Ni, and Co have similar stabilities in the dissolution reactions except for reaction 3, for which Ni and Co having similar stabilities are the most unstable, and Pd and Rh behave similar to each other and more stable that Ni and Co, but still strongly unstable with respect to Pt and Ir. Thus, the similarity between Figure 3.1b and Figure 3.3 indicates that the relative stabilities of second metals in Pt-based bimetallic alloys correlate well with the stabilities of the corresponding pure metal cathode catalysts in the same acidic environment.

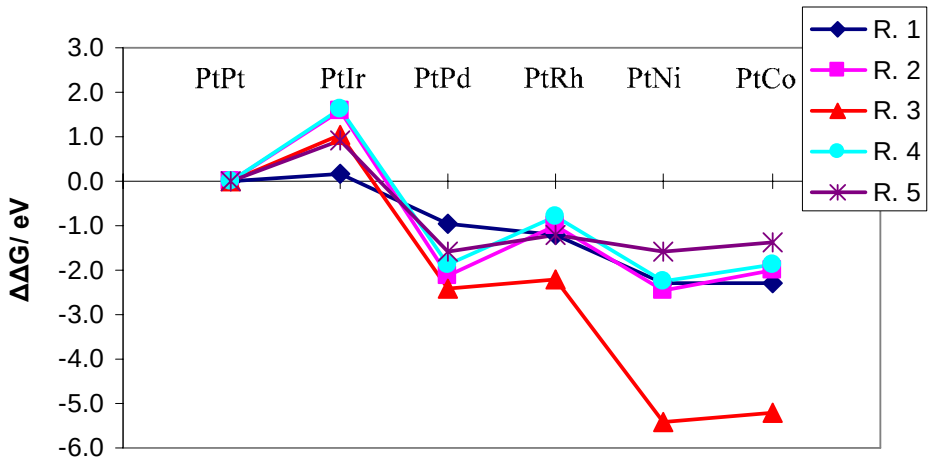

Figure 3.3. $\Delta\,\Delta G$ (eV) of Pt, Pd, Ni, Ir, Rh, and Co dissolution reactions in Pt alloys. $\Delta\,\Delta G$ s of PtPt, PtPd, PtNi, PtIr, PtRh, and PtCo alloy cathode catalyst are based on $M(H_2O)_6^{2+}$ with B3LYP/LANL2DZ and 6-311++g(d,p).

3.5. Comparison of Pt and Alloyed Metal Stabilities against Dissolution in the Same Pt-based Bimetallic PtM Alloys. The results shown in Figure 3.4 are based on the values of $\Delta\Delta G$, defined as $\Delta\Delta G = \Delta G_1 - \Delta G_2$, where ΔG_1 is the free energy for the second species M as adsorption site in each dissolution reaction for a PtM alloy, and ΔG_2 is the free energy for Pt as adsorption site in PtM in each dissolution reaction. Therefore, the negative $\Delta\Delta G$ indicates that the Pt site is more stable than those of the second metal species in Pt-based bimetallic cathode catalysts assuming that both Pt and the other metal species are able to act as adsorption sites for O, OH, and OOH. Certainly the $\Delta\Delta G$s are zero for PtM = PtPt. Figure 3.4 shows that Ir is more stable than Pt in the PtIr alloy cathode catalyst due to the positive $\Delta\Delta G$ values in all five dissolution reactions. Metal Co is also more or equally stable than Pt in the PtCo alloy except in reaction 3. Pd, Rh, and Ni are less stable than Pt in PtPd, PtRh and PtNi alloy cathode catalysts respectively which is consistent with the experimental report that Pd and Rh are more soluble than Pt in acid environment[50].

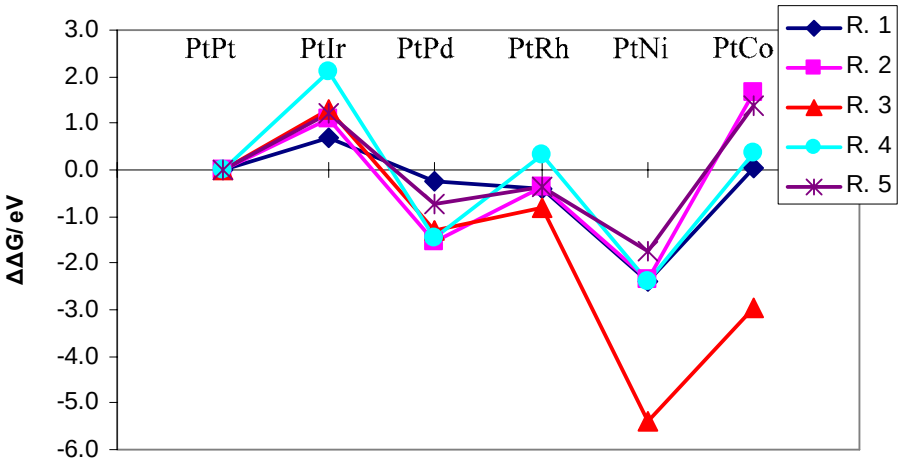

Figure 3.4. $\Delta\Delta G$ (eV) of dissolution reactions of Pt vs. Pt, Pd, Ni, Ir, Rh, and Co in Pt alloys. $\Delta\Delta G$s of PtPt, PtPd, PtNi, PtIr, PtRh, PtCo alloy cathode catalyst are based on $M(H_2O)_6^{2+}$ with B3LYP/Lanl2dz and 6-311++g(d,p)

3.6. Summary. Analyses of the calculated ΔGs of possible dissolution reactions involving adsorbed oxygen reduction intermediates indicate that five dissolution reactions of oxygen reduction reaction catalysts are thermodynamically favorable. Those cathode catalyst dissolution reactions are electrochemical instead of chemical reactions. The relative stabilities against dissolution of different pure metal cathode catalysts (Pt, Ir, Pd, Rh, Ni, Co) with respect to Pt based on the $\Delta\Delta$G for each dissolution reaction indicate that Ir is the most stable pure catalyst.

For alloy cathode catalysts, the introduction of a second metal influences the Pt stability in the alloy catalysts, except for Ni which has little influence on the Pt stability in a PtNi alloy compared with the stability of Pt in pure Pt catalyst. The presence of Ir, Pd, Rh, and Co decreases the stability of Pt in PtIr, PtPd, PtRh and PtCo respectively compared with Pt in a pure Pt cathode catalyst.

The relative stabilities of Ir, Pd, Rh, Ni, Co in the corresponding alloy cathode catalysts show similar trends as those of the corresponding pure cathode catalysts, Ir (in Pt-Ir) being the most stable. Comparing the relative stabilities to a given dissolution reaction of Pt and another metal species in the same alloy cathode catalyst, it is found that Ir and Co are more stable than Pt in PtIr and PtCo respectively.

CHAPTER IV

ABSORPTION OF ATOMIC OXYGEN INTO SUBSURFACES OF PT(100) AND PT(111)

As mentioned in introduction chapter, the electrochemical literature describes in great detail the observation of an apparent connection between oxide growth stages detected approximately between 0.8 V and 1.2 V (measured with respect to the hydrogen electrode potential) and the dissolved Pt concentration[57] for a Pt electrode in acid medium. Atomic oxygen can be found in the subsurface of transition metals during surface reactions in various experimental environments[61-66] and subsurface oxygen may be further considered as the initial stage in the corrosion and growth of metal oxides[70]. Under electrochemical conditions the subsurface oxygen can be formed in the oxidation of polycrystalline platinum and the concentration of subsurface oxygen has been found to depend on the cycling rate by cyclic voltammetry experiments[71,72]. However, the microscopic understanding of this complex process is at its infancy. In this chapter we present the first of a series of studies tending to investigate the adsorbed on-surface oxygen migration into subsurface. Our calculations are done on Pt(100) and Pt(111) surfaces. We characterize the site preference of an oxygen atom adsorbed on Pt(111) and Pt(100) surfaces as a function of coverage, the absorption of atomic oxygen inside Pt(111) and Pt(100) subsurfaces, and the migration of an oxygen atom from low surface coverage into the subsurface.

4.1. Oxygen Atom Adsorption on Pt Surfaces. Experimental investigations have shown that the most favorable atomic oxygen adsorption site on Pt(111) surfaces is the three-fold site and the adsorption energies vary with coverage[110]. We explore the most stable adsorption sites on both Pt(100) and Pt(111) surfaces by comparing the binding energies calculated by following equation at various surface coverages.

$$E = E_{Pt_nO} - E_{Pt_n} - E_O$$

Figure 4.1 shows three adsorption sites: top, bridge and hollow on Pt(100) and on Pt(111) surfaces. On a Pt(111) surface there are two types of hollow sites: *fcc*, under which there is no Pt atom in the second layer, and *hcp*, under which there is a Pt atom (Figure 4.2).

Table 4.1 shows the binding energies of oxygen on Pt surface sites at 0.25ML surface coverage. The data in Table 4.1 indicates that the oxygen atoms prefer binding to the high-coordinated hollow sites on the Pt(111) surface, and that the *fcc* hollow site is slightly more stable than the *hcp* site by 0.4 eV binding energy difference, in agreement with scanning tunneling microscopy (STM) results indicating that oxygen atoms resulting from dissociation of the molecular precursor state locate on upper sites of Pt step edges occupying *fcc* sites.[111] Thus, the most energetically stable site for atomic oxygen adsorption on a Pt(111) surface is *fcc*. Both binding energies of 4.61 eV and 4.21 eV on *fcc* and *hcp* respectively agree with experimental values of atomic oxygen adsorption energy on Pt(111) surface of 4.32 eV[110] and the calculated Pt-O bond lengths of 2.04 and 2.05 Å at *fcc* and *hcp* sites respectively also agree with experimental values of 2.01±0.05 Å on Pt(111)[112].

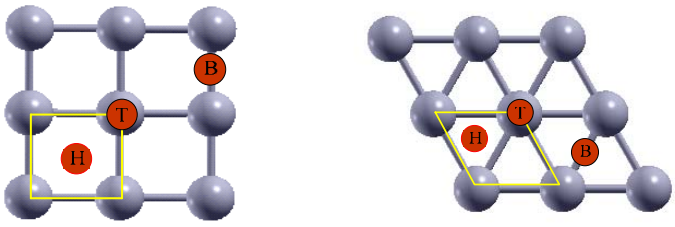

a b

Figure 4.1. Oxygen atom adsorption sites on Pt(100)/(a) and Pt(111)/(b) surfaces. H, B, T denote hollow, bridge and top sites respectively. Primitive surface (1×1) cells of Pt(100) and Pt(111) are shown (yellow).

Table 4.1: Binding energies (E_b, in eV) and Pt-O bond lengths (L_b, in Å) of atomic oxygen on Pt(111) and Pt(100) surfaces with coverage of 0.25 ML.

Surface		Pt(111)				Pt(100)		
Site		*fcc* H	*hcp* H	B	T	B	H	T
Coordination		3	3	2	1	2	4	1
0.25ML	E_b	-4.61	-4.21	-3.97	-3.21	-4.62	-4.31	-3.56
	L_b	2.04	2.05	1.99	1.84	1.95	2.22	1.82

H, B, T denote hollow, bridge and top sites respectively.

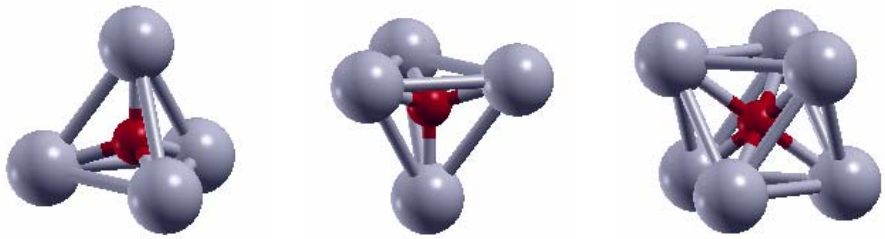

(a) Pt(111): (I) tetrahedral/tetra-I; (II) tetrahedral/tetra-II; (III) octahedral/octa

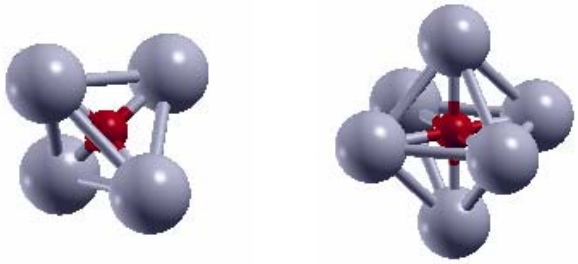

(b) Pt(100): (I) tetrahedral/$tetra_{100}$; (II) octahedral/$octa_{100}$

Figure 4.2. Pt(111) and Pt(100) subsurface sites for oxygen atom absorption. Red denotes oxygen and light blue denotes platinum.

Table 4.1 also shows the binding energies on different sites of a Pt(100) surface, indicating that the bridge site is the most energetically favorable site for oxygen atom

adsorption, being more stable than higher coordination hollow sites, though the difference of binding energies is pretty small. Comparing bond lengths and coordination numbers of the respective sites of Pt-O on both Pt(111) and Pt(100) surfaces, we find that both coordination number and bond lengths influence the binding energy of oxygen atom adsorption on Pt surfaces. Though the Pt-O bond lengths at hollow sites on Pt(111) are larger than those on top and bridge, hollow sites with coordination number of 3 have stronger (more negative) binding energies. Whereas, even when the coordination number is 4 on the hollow site of Pt(100), oxygen atoms prefer to attach to bridge sites on which the Pt-O bond lengths are much shorter than on hollow sites. The binding energies of oxygen at the preferred *fcc* sites on Pt(111) and bridge on Pt(100) are almost the same: 4.61 and 4.62 eV respectively at 0.25 ML coverage.

Oxygen atom coverage effects on the binding energy of oxygen are shown in Table 4.2. Since the difference of binding energies at *fcc* and *hcp* hollow sites of the Pt(111) surface is small, we listed the binding energies for the two adsorption sites, and similarly for bridge and hollow sites of the Pt(100) surface. Table 4.2 shows that the binding energy generally becomes less negative with the increasing of the coverage from 0.11 ML to 1.00 ML at each adsorption site, although maximum binding energies are found at 0.25 ML for hollow *fcc* and hollow sites in the Pt(111) and Pt(100) surfaces respectively. The binding energies of oxygen atom adsorption at *fcc* and *hcp* sites on Pt(111) at high coverage (1.00 ML) are 1.0 eV less negative than that of lower coverage (0.11 ML), which indicates that repulsion among oxygen atoms at higher coverage (1.00 ML) is significant. The *fcc* hollow site is always more stable than the *hcp* site for oxygen adsorption in the range of coverage from 0.11 to 1.0 ML on Pt(111) according to the calculated binding energies.

At the hollow site on Pt(100) surface, repulsion among oxygen atoms at 1.0 ML coverage is also significant based on the binding energy approximately 1.0 eV less negative than that of 0.11 ML coverage. At the bridge site on Pt(100), the binding energy differs slightly (~0.11 eV) between 0.11 ML and 0.50 ML. Even at the 1.0 ML coverage, the bridge binding energy is 0.51 eV less negative than that of 0.11 ML

coverage, which may be explained on the basis that tighter binding overcomes the repulsion effects to some extent. The bridge site is always more stable than the hollow site on Pt(100) surface for oxygen atom adsorption at the same coverage. The binding energies on Pt(100) and Pt(111) are similar at the most stable sites at the same coverage, especially at low coverage they differ by around 0.1 eV, though the surface energy of Pt(100) is slightly lower than that of Pt(111)[113].

Table 4.2: Binding energies (E_b, in eV) of atomic oxygen adsorption at *fcc* and *hcp* hollow sites on Pt(111) and at bridge and hollow sites on Pt(100) surface with coverage of 0.11 ML, 0.25 ML, 0.50 ML, 1.00 ML. H, B denote hollow and bridge sites.

Surface coverage	E_b in Pt(111)		E_b in Pt(100)	
	fcc H	*hcp* H	B	H
0.11 ML	-4.59	-4.29	-4.71	-4.22
0.25 ML	-4.61	-4.21	-4.62	-4.31
0.50 ML	-4.35	-4.16	-4.60	-3.96
1.00 ML	-3.59	-3.18	-4.20	-3.17

4.2. Oxygen Atom Absorption inside the Pt Subsurface. As mentioned in the introduction section, subsurface oxygen was detected during transition metal surface oxidation for Pt[61,63,71,72] and Ru[64,65] by a variety of structural and spectroscopic techniques in various experimental environments. In this section we analyze subsurface oxygen absorption under Pt(111) and Pt(100) surfaces at zero and low surface coverages. Figure 4.2 shows the subsurface sites of Pt(111) and Pt(100) surfaces for oxygen absorption. There are three types of subsurface sites for atomic oxygen absorption between the first layer (top layer) and the second layer of Pt(111) surfaces: one is an octahedral site located underneath an *fcc* hollow site; the other two are tetrahedral sites designated as tetra-I and tetra-II corresponding to underneath top and *hcp* hollow sites

respectively. For Pt(100) subsurface sites, there is one tetrahedral site between the first and second layer underneath a bridge site and another one is an octahedral site located among the top three layers, underneath a top site.

Table 4.3: Absorption energy (E_{ab}, in eV) of the oxygen atom inside subsurface sites in Pt(111) and Pt(100) surface cells with subsurface coverages of 0.11 ML, 0.25 ML, at zero surface coverage.

Subsurface coverage	E_{ab} in Pt(111)			E_{ab} in Pt(100)	
	octa	tetra-I	tetra-II	$octa_{100}$	$tetra_{100}$
0.11 ML	-0.76	-1.88	-2.81	-0.29	-2.71
0.25 ML	-1.80	-1.68	-2.66	-0.39	-2.32

Table 4.3 shows the absorption energies of the oxygen atom inside the subsurface sites at subsurface coverages of 0.11 ML and 0.25 ML (and zero surface coverage), calculated using above equation in section 4.1. The tetrahedral site (tetra-II) underneath a *hcp* surface site (Figure 4.2) is the most stable site for oxygen lodging in the Pt(111) subsurface at both 0.11 ML and 0.25 ML subsurface coverage based on the absorption energies. The absorption energies in the other two sites are almost 1.0 eV less negative than that of tetra-II site. As the subsurface coverage increases from 0.11 ML to 0.25 ML, the absorption energy becomes less negative by 0.15 eV in tetra-II sites. An interesting point is that the absorption energy in the octahedral site at 0.11 ML coverage is much less negative than that at 0.25 ML, which indicates that an oxygen atom absorbed in the octahedral site becomes stabilized at higher subsurface coverage.

For the Pt(100) surface, the tetrahedral site ($tetra_{100}$) underneath a bridge site (Figure 4.2) is the most favorable site with much more negative absorption energy (by ~ 2.0 eV) than that of the octahedral ($octa_{100}$) at subsurface coverage of 0.11 ML and 0.25 ML. According to the absorption energies in the octahedral site of Pt(100) (-0.29 eV at

0.11ML; -0.39 eV at 0.25ML), an oxygen atom absorbed inside the octahedral site is much energetically unstable. Similarly to the Pt(111) surface, with increasing subsurface coverage, the absorption energy becomes less negative in the tetrahedral site of Pt(100), which indicates that oxygen repulsion decreases subsurface absorption at higher subsurface coverage (and zero surface coverage). In summary, tetra(II) and $tetra_{100}$ are the most stable sites for oxygen atom absorption into Pt(111) and Pt(100) subsurfaces respectively at these conditions. We note that absorption in the subsurface may be strongly dependent on the surface coverage[114]. In this chapter, we present our studies to subsurface absorption at zero and low surface coverage.

Figure 4.3 shows the thermodynamically most stable oxygen absorption structures in Pt(111) tetra-II and Pt(100) tetra subsurface sites at 0.11 ML coverage. Absorbed oxygen causes distortion of the top surface, in which Pt atoms coordinated with subsurface oxygen are pushed up in the direction of the vacuum space (see for example Figure 4.3b). We characterize these distortions defining a vertical distance (D_{PtPt}) between a Pt atom in the first layer bonded to a subsurface oxygen atom, and the horizontal line defined by the Pt atom nearest neighbors in the same top layer. Table 4.4 shows that the D_{PtPt} vertical distortion distance (D_{PtPt}) decreases from 0.31 Å to 0.28 Å in Pt(111) and from 0.52 Å to 0.43 Å in Pt(100) as the coverage decreases from 0.25 ML to 0.11 ML, which can explain why the absorption energy becomes more negative with decreasing coverage from 0.25 ML to 0.11 ML in stable sites (Table 4.3). The higher the distortion, the less negative absorption energy is. Table 4.4 also shows the vertical distance (D_{OPt}) between the oxygen atom and the Pt atoms in the top layer that are coordinated with such subsurface oxygen. With the increasing of coverage from 0.11 to 0.25 ML, the atomic oxygen goes deeper away from the top layer from 0.36 to 0.78 Å, and from 0.87 to 1.24 Å in Pt(111) and Pt(100) stable subsurface sites respectively. This observation indicates that stronger repulsion between subsurface oxygen atoms at higher subsurface coverage makes the atomic oxygen to reside in deeper positions and that subsurface atomic oxygen closer to the top layer at lower subsurface coverage causes less vertical interlayer distortion of Pt atoms in the top layer.

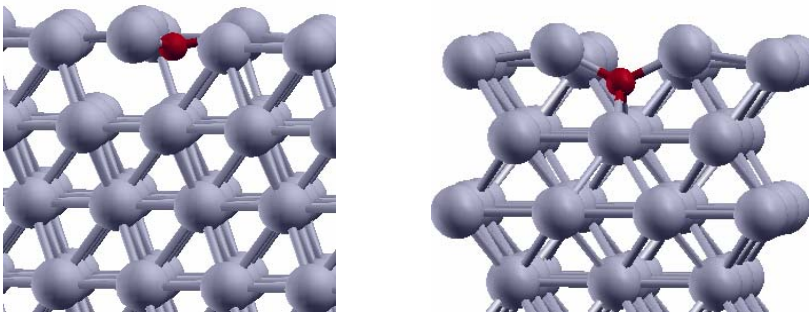

(a) (b)

Figure 4.3. Most stable absorption structures of atomic oxygen in Pt(111) and Pt(100) subsurfaces at 0.11 ML subsurface coverage (zero surface coverage). Pt atoms in light blue, O atom in red. (a) tetra-II site in Pt(111); (b) $tetra_{100}$ site in Pt(100).

Table 4.4: Vertical distortion distance (D_{PtPt}/ Å) between Pt atoms in the top layer and vertical distance (D_{OPt}/ Å) between the subsurface oxygen atom and Pt atoms in the top layer of Pt(111) and Pt(100) surface cells coordinated with this oxygen atom.

		Tetra-II/Pt(111)	$Tetra_{100}$/Pt(100)
0.11 ML	D_{PtPt}	0.28	0.43
0.25 ML		0.31	0.52
0.11 ML	D_{OPt}	0.36	0.87
0.25 ML		0.78	1.24

The first column indicates the various subsurface coverages.

4.3 Diffusion of Atomic Oxygen from the Surface to the Subsurface. In the above two sections we discussed the stable sites of atomic oxygen on Pt surfaces and in Pt subsurfaces. The minimum energy path (MEP) for the oxygen atom diffusion into subsurfaces at 0.25 and 0.11 ML surface coverage calculated by the climbing image

nudged elastic band method[105-107] is reported in this section. Atomic oxygen diffusion from Pt(111) surface into the subsurface was investigated starting from the most stable *fcc* site. Figure 4.4 shows the MEP of the absorption process of atomic oxygen into Pt(111) subsurface. An oxygen atom adsorbed on *fcc* site first migrated to the *hcp* site (point B) across the bridge site (point A), in which the energy barrier is 0.63 eV and the oxygen on bridge site is the transition state. After reaching the *hcp* site (point B), the oxygen atom begins to diffuse inside the subsurface (Figure 4.4). During this process, the Pt-O bond distance (R_{PtO}) and the vertical distance (D_{PtO}) between the adsorbed oxygen and the top Pt layer decreased before the transition state, whereas, the Pt bond distance (R_{PtPt}) in *hcp* increased considerably during the diffusion of oxygen into the subsurface (Table 4.5). At the transition state the oxygen atom becomes almost lodged in the surface *hcp* site coordinating with three Pt atoms (point C in Figure 4.4) and the distortion reached its maximum. The energy barrier of absorption atomic oxygen from *hcp* to tetra-II is 2.22 eV and the reverse energy barrier is 0.70 eV, which indicates that the equilibrium constant for producing subsurface oxygen at this low surface coverage- is pretty small. The energy difference between the *fcc* and tetra-II is 1.93 eV, which also indicates that the atomic oxygen atom that stays on the surface is thermodynamically more stable. Figure 4.5 shows the MEPs from *hcp* to tetra-II at the coverages of 0.25ML and 0.11 ML respectively. At the lower coverage of 0.11 ML, the energy barrier for absorption (1.41 eV) is lower than that at 0.25 ML (2.22 eV). However, the reverse energy barrier is almost zero, which indicates that the subsurface oxygen almost can not exist at the lower coverage. This observation is consistent with the above analysis that oxygen is closer to the top layer at 0.11 ML coverage than at 0.25 ML.

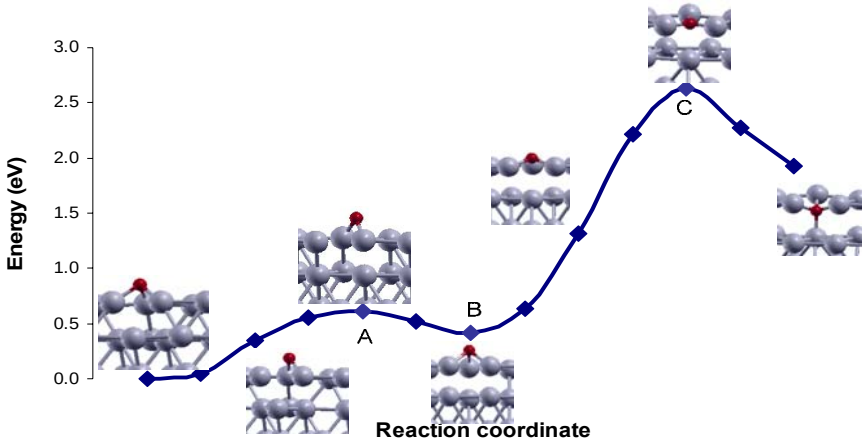

Figure 4.4. Minimum energy path of atomic oxygen diffusion from the *fcc* surface to the subsurface tetrahedral/tetra-II site in Pt(111) surface cell at surface coverage 0.25 ML. O in red; Pt in light blue. The evolution of the main distances from the hcp (point B) to the subsurface oxygen (tetra II) is indicated in Table 4.5. The PtO distance decreases as O moves from point B to point C (transition state) and then increases slightly as O moves into the tetra II site. The vertical distance between O and the top layer decreased from B to C (where it reaches a minimum value) and then increased again as O moves deeper into the subsurface (Table 4.5). The Pt-Pt distance becomes elongated as the oxygen atom descends into the subsurface; the distortion is a maximum at the transition state (C).

Table 4.5: Variation of Pt-O bond length (R_{PtO}), vertical distance (D_{PtO}) of oxygen to Pt-top layer, bond between Pt atoms (R_{PtPt}) in the top layer which coordinate with O along the MEP, in Pt(111) cell at 0.25 ML[a].

No.	*hcp*	1	2	3	4 (C)	5	Tetra-II
R_{PtO}	2.06	1.98	1.91	1.86	1.85	1.89	1.96
D_{PtO}	1.22	0.94	0.61	0.26	-0.10[b]	-0.46[b]	-0.78[b]
R_{PtPt}	2.87	3.03	3.13	3.19	3.21	3.18	3.12

[a] Distances in Å. Numbers from 1 to 5 correspond to points from left to right in Figure 4 between *hcp* (point B in Figure 4) to tetra-II. Point 4 (C in Figure 4) is the transition state.
[b] Negative means the oxygen beneath the Pt top layer.

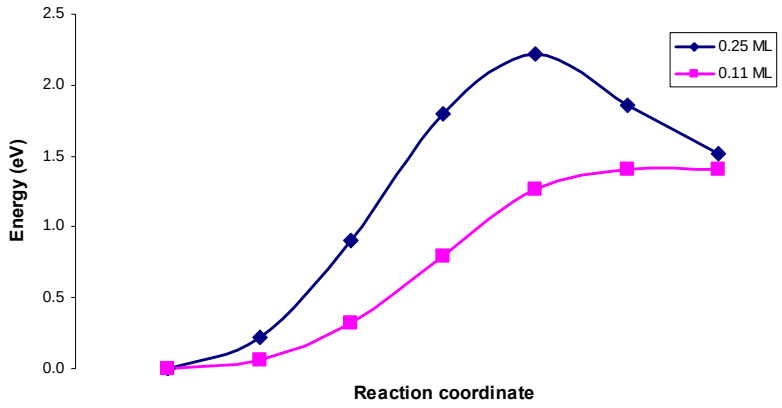

Figure 4.5. Minimum energy path of atomic oxygen diffusion from *hcp* surface to subsurface tetrahedral/tetra-II site in a Pt(111) surface cell at surface coverages 0.25 ML and 0.11ML.

Atomic oxygen adsorption at bridge and hollow sites on the Pt(100) surface have similar binding energies, therefore the MEPs from each of the two sites diffusing into tetra sites in the Pt(100) subsurface were also studied. Figure 4.6a shows the MEP from hollow to $tetra_{100}$ at 0.25 ML. During the diffusion process illustrated in Figure 4.6a, the oxygen atom becomes close to two of the four Pt atoms which form the hollow site, and at the same time the oxygen migrates into the subsurface before evolving to the transition state. This evolution can be monitored by changes in Pt-O bond (R_{PtO}) and dihedral angle O-Pt-Pt-Pt ($D_{OPtPtPt}$) shown in Table 4.6a. At the transition state, the oxygen resides in the triangular plane formed by three Pt atoms, and both the vertical distortion of the top layer (D_{PtPt}) and $D_{OPtPtPt}$ reach maximum values, whereas R_{PtO} passes through a minimum value (Table 4.6a). The energy difference between atomic oxygen on hollow and in $tetra_{100}$ is 2.0 eV, which indicates that thermodynamically the atomic oxygen prefers lodging on the surface. The energy barrier of diffusion from the surface into the subsurface is 2.46 eV and the reverse diffusion energy barrier is 0.43 eV, indicating that the equilibrium constant for producing subsurface oxygen is very small. Figure 4.6b shows the atomic oxygen diffusion from bridge into subsurface $tetra_{100}$ site

at 0.25 ML. During the diffusion process, the oxygen atom inserts into the bridge site which is formed by two Pt atoms, then goes into the $tetra_{100}$ site (Figure 4.6b, changes in structural parameters listed in Table 4.6b). The energy difference between bridge and $tetra_{100}$ is 2.30 eV, which is also thermodynamically unfavorable. The energy barrier from bridge to $tetra_{100}$ is 4.40 eV which is much larger than the barrier of 2.46 eV from hollow to $tetra_{100}$. The energy difference of 0.3 eV between bridge and hollow sites on surface is small, which indicates that oxygen migration from bridge to hollow is comparatively easier. Therefore, diffusion into the subsurface would be more favorable from hollow than from bridge site of the Pt(100) surface.

Table 4.6: Variation of Pt-O bond length (R_{PtO}), vertical distortion distance (D_{PtPt}) of Pt top layer (see text), bond between Pt atoms (R_{PtPt}) which coordinate with O, dihedral angle ($D_{OPtPtPt}$) along the MEP in Pt(100) cell at 0.25 ML.[a]

(a)

No.	hollow	1	2	3	4	5	tetra
R_{PtO}	2.22	2.02	2.00	1.98	1.97	2.01	2.02
D_{PtPt}	0.00	0.20	0.40	0.59	0.78	0.67	0.52
$D_{OPtPtPt}$	36.3	40.3	16.0	-11.2*	-109.7*	-90.7*	-79.6*

(b)

No.	bridge	1	2	3	4	5	tetra
R_{PtO}	1.95	1.87	1.78	1.73	1.74	1.87	2.02
R_{PtPt}	2.93	3.17	3.34	3.43	3.44	3.31	3.20
D_{PtPt}	0.17	0.15	0.38	0.51	0.66	0.76	0.52
D_{PtO}	1.29	0.99	0.61	0.20	-0.18[b]	-0.89[b]	-1.24[b]

[a] Distances in Å; angle in °. (a) hollow to $tetra_{100;}$ numbers from 1 to 5 correspond to points in Figure 4.6(a) from left to right between hollow and $tetra_{100}$. (b) bridge to $tetra_{100}$; numbers from 1 to 5 correspond to points in Figure 4.6(b) from left to right between bridge and $tetra_{100}$.

[b] Negative means the oxygen beneath the Pt top layer.

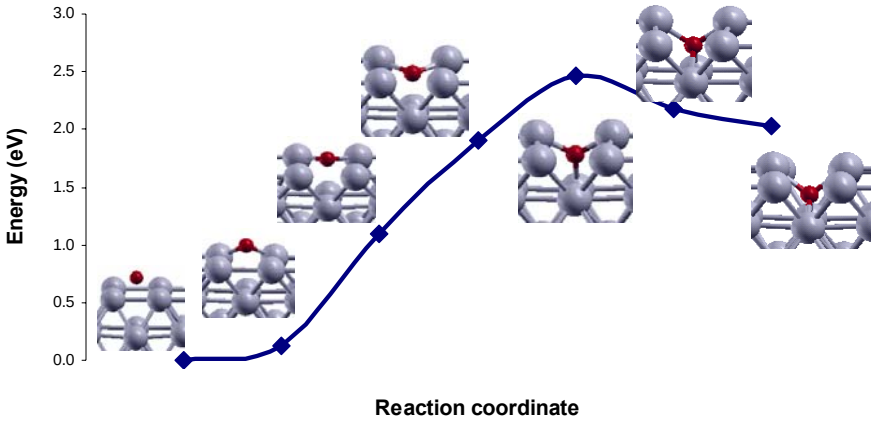

(a)

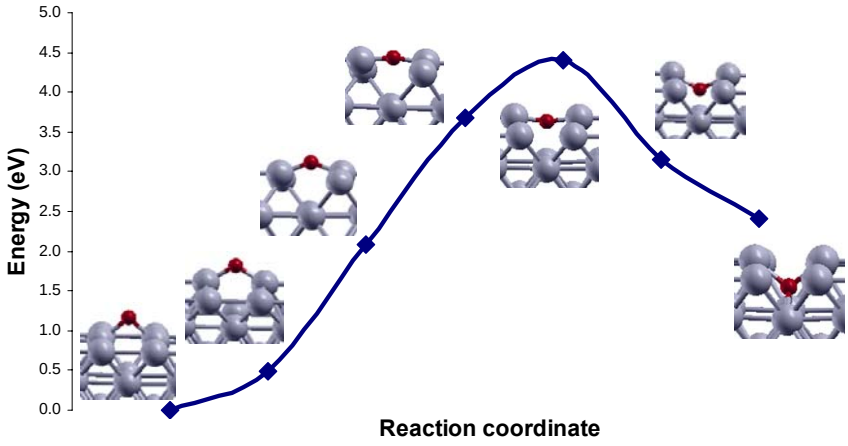

(b)

Figure 4.6. Minimum energy path of atomic oxygen diffusion from surface to subsurface tetrahedral site in Pt(100) surface cell at 0.25 ML surface coverage. (a) hollow to $tetra_{100}$; (b) bridge to $tetra_{100}$. O in red; Pt in light blue. The evolution of the main distances is indicated in Tables 4.6(a) and 4.6(b) respectively.

4.4. Summary. Spin polarization DFT calculations show that the most stable adsorption sites on Pt(111) and Pt(100) surface are *fcc* hollow and bridge respectively. Increasing surface coverage, the binding energies become less negative due to increased

oxygen repulsion. The most stable subsurface site of Pt(111) cell is the tetrahedral/tetra-II site underneath a *hcp* hollow site. The tetrahedral/$tetra_{100}$ site underneath a bridge site is the most stable site in the Pt(100) subsurface at zero surface coverage. Also increasing subsurface coverage the absorption energy becomes less negative and atomic oxygen lodges deeper away from the top layer.

Atomic oxygen endothermic absorption into the Pt(111) subsurface -at low surface coverages- follows this minimum energy path: it migrates from *fcc* to *hcp* site with an energy barrier of 0.63 eV where the transition state geometry has the oxygen at a bridge site; then the oxygen atom diffuses into the subsurface tetra-II site from the hcp site with an energy barrier of 2.22 eV and a reverse barrier of 0.70 eV with the atomic oxygen in hcp site as the transition state. For the atomic oxygen endothermic absorption into the Pt(100) surface we found minimum energy paths from hollow to $tetra_{100}$ and from bridge to $tetra_{100}$. The MEP of hollow to $tetra_{100}$ has smaller energy barrier (2.46 eV) than that of bridge to $tetra_{100}$ (4.4 eV). At lower coverage of 0.11ML, the absorption energy barrier on Pt(111) decreases, however, the reverse energy barrier is close to zero, indicating that the subsurface oxygen hardly exists under low surface coverage conditions.

Finally, note that the equilibrium platinum dissolving concentration is very small, in the range of 10^{-9} to 10^{-6} M, measured at various conditions [57]. Therefore, the corrosion controlling elementary step could have very unstable intermediates, also could have high activation energy to produce unstable corrosion intermediates, with small reverse activation energy. If the cathode catalyst would have low activation energy for corrosion, it would not last as the oxygen reduction reaction cathode catalyst in fuel cells. Atomic oxygen penetrating into the subsurface could be the one of elementary steps of platinum cathode corrosion and dissolution; even it could be the controlling step of the whole corrosion process. As indicated in the introduction, we emphasize the need of surface science studies (experimental and computational) on single crystal surfaces which can provide fundamental information about the dissolution mechanism in the same way that binding energies of oxygenated compounds calculated on single crystal surfaces (gas

phase studies, no electrode potential incorporated) correlate amazingly well with electrochemical reduction currents.

CHAPTER V

CHEMICAL ENVIRONMENT EFFECTS ON THE ATOMIC OXYGEN ABSORPTION INTO PT(111) SUBSURFACES

In previous chapter the minimum energy path for atomic oxygen absorption into subsurface was investigated from the most energetically favorable fcc on-surface three fold site to the Pt(111) subsurface tetrahedral site (tetra-II). Meanwhile the atomic oxygen binding energies on Pt(111) surface decrease with the surface coverage increasing. In this chapter we present the oxygen and OH surface coverage and water solution effects on the atomic absorption process such as minimum energy path and absorption energy barrier.

5.1. Atomic Oxygen Coverage Effect on the Oxygen Absorption. In previous work we found that the diffusion process from surface to subsurface yielding 0.11 ML and 0.25 ML subsurface coverage at zero on-surface atomic oxygen is energetically unfavorable and the energy barrier for such process is lower at the lowest subsurface coverage[115]. In this work we calculated (Table 5.1) the surface coverage effect on the energetics of the absorption process at the same subsurface coverage of 0.11 ML and 0.25 ML respectively. We define ΔE as the energy difference between two systems of the same total oxygen coverage: the first system (energy E_{sub}) with certain oxygen coverage in the subsurface and the difference (total coverage – subsurface coverage) on the surface, and the second system (energy E_{on}) with all oxygen coverage on the surface, $\Delta E = E_{sub} - E_{on}$. Table 5.1 shows that ΔE decreases with increasing on-surface coverage (total coverage – subsurface coverage) both for 0.11 ML and 0.25 ML subsurface coverage, which indicates that increasing on-surface oxygen coverage stabilizes the subsurface oxygen to some extent. At subsurface coverage of 0.11 ML, ΔE drops fast from 1.19 eV to 0.39 eV going from total coverage of 0.67 ML to 0.78 ML and it becomes negative at 1.00 ML total coverage (on-surface coverage of 0.89 ML). At total coverage smaller than 0.67 ML, the decrease of ΔE is less pronounced than that between 0.67 and 0.78 ML. Therefore, at 0.11 ML subsurface coverage, the on-surface oxygen

stabilizing effect on subsurface oxygen starts to become apparent when the total oxygen coverage is ≥ 0.78 ML (on-surface oxygen coverage ≥ 0.67 ML).

Table 5.1: Energy difference (ΔE, in eV) at constant total coverage between systems with and without subsurface oxygen.[a]

0.11 ML atomic oxygen in subsurface:									
Coverage/ML	0.00/0.11	0.11/0.22/	0.22/0.33	0.33/0.44	0.44/0.56	0.56/0.67	0.67/0.78	0.78/0.89	0.89/1.00
ΔE/ eV	1.83	1.84	1.61	1.45	1.41	1.19	0.39	0.16	-0.38
0.25 ML atomic oxygen in subsurface:									
Coverage/ML	0.00/0.25		0.25/0.50		0.50/0.75		0.75/1.00		
ΔE/ eV	1.99		0.79		0.13		-0.35		

[a] The oxygen coverage is indicated as "on-surface coverage/total coverage". The first two rows correspond to 0.11 ML and the last two to 0.25 ML subsurface oxygen.

In contrast, at 0.25 ML subsurface oxygen, ΔE decreases faster at small total coverage than that at comparatively higher coverage (a drop of 1.2 eV from 0.25 ML to 0.50 ML compared to a decrease of 0.68 eV from 0.50 ML to 0.75 ML), thus the on-surface oxygen stabilizing effect on subsurface oxygen increases faster at total coverage smaller than 0.50 ML. The stabilizing effect on subsurface oxygen at 0.25 ML (Table 5.1) becomes clear with the surface coverage increasing, as indicated by the decreasing ΔEs and it is found that at a total coverage of 1 ML (0.75 surface coverage) the absorption process becomes energetically favorable. Comparing the value of ΔE for the two values of subsurface oxygen coverage (Table 5.1) at similar on-surface oxygen coverage, it is found that the subsurface oxygen is more stable at 0.25 ML than at 0.11 ML; for example, ΔE is -0.35 eV with 0.75 ML on-surface oxygen at 0.25 ML subsurface oxygen, whereas the ΔE value is positive (0.39 eV) at 0.11 ML subsurface coverage and 0.78 ML on-surface coverage. In summary, the on-surface oxygen stabilizes the subsurface oxygen energetically and the effect becomes more marked at

higher on-surface oxygen coverage. The rate of increase of such stabilizing effect is also faster at 0.25 ML than at 0.11ML subsurface coverage.

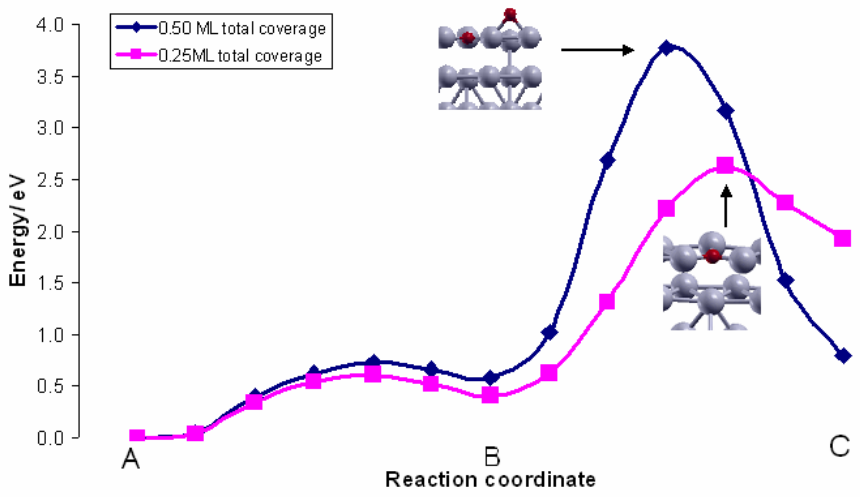

Figure 5.1. Minimum energy paths of oxygen absorption into the Pt(111) subsurface with 0.25 ML oxygen migration into the subsurface at 0.50ML and 0.25 ML total coverage. A: fcc hollow site; B: hcp hollow site; C: subsurface tetrahedral site.

Figure 5.1 shows the minimum energy paths for 0.25 ML oxygen migration into the Pt(111) subsurface at two different *total* oxygen coverages: 0.25 ML and 0.5 ML. As reported earlier[115], the oxygen first migrates from the fcc hollow site (point A) to the hcp hollow site (point B) through a bridge site, then the oxygen atom begins to diffuse into the subsurface site (tetrahedral site beneath hcp hollow site, point C). A first transition state is located when the atomic oxygen migrates to the hcp hollow site (Figure 5.1). With the total oxygen coverage increasing from 0.25 to 0.5 ML layer, the energy barrier of on-surface diffusion from fcc site to hcp site also increased from 0.61 eV to 0.73 eV, whereas, the reverse energy barrier decreased from 0.20 eV to 0.14 eV. The barrier for diffusion from fcc to hcp is in good agreement with earlier reports.[116] Thus, with the

total coverage increasing, the on-surface diffusion energy barrier increased and the reverse energy barrier decreased, which indicates that higher total oxygen coverage makes the oxygen diffusion to the hcp site more difficult and unstable from kinetic and energetic points of view. For the oxygen migration from the hcp site into the subsurface tetrahedral site, the energy barrier at 0.50 ML *total* oxygen coverage is 3.18 eV which is much higher than that at *total* oxygen coverage 0.25 ML (2.22 eV). The reverse energy barrier of absorption at 0.50 ML *total* coverage is 2.98 eV, much larger than that at *total* coverage 0.25 ML (0.70 eV). From these observations, the increasing *total* oxygen coverage produces a huge increase of the energy barrier for migration from hcp to the subsurface. On the other hand, the reverse energy barrier increased with the increase of the *total* oxygen coverage so that the subsurface oxygen could be kinetically more stable at higher coverage. The increase of the energy barrier for the forward reaction (from hcp site B in Figure 5.1 to the transition state between B and C) at higher *total* oxygen coverage can be explained by the larger lattice deformation (See Table 5.2) required at higher total coverage. For example, at 0.50 ML total coverage, the change in each Pt-Pt bond length for the Pt atoms coordinated to O at the hcp and at the transition state sites is 0.362 Å; i.e., in average the bond lengths change from 2.794 to 3.156 Å, whereas the equivalent change at 0.25 ML is 0.333 Å. Substantial lattice deformation is also required for the reverse process: diffusion of O from the subsurface site C to the transition state in Figure 5.1, the change in Pt-Pt bond length at 0.50 ML is of 0.297 Å compared with 0.091 Å at 0.25 ML. Also, at 0.50 ML the oxygen lodges deeper in the subsurface (1.293 Å from the Pt top layer) than at 0.25 ML (1.215 Å), that together with on-surface increased repulsive O-O interactions will make the reverse process more difficult than at the lower 0.25 ML total coverage.

Table 5.2: DFT calculated Pt-O bond distance (R_{PtO}) between subsurface absorbed O and Pt atoms in the top layer, Pt-Pt bond length (R_{PtPt}) at the hcp site in the top layer which coordinates with absorbed O, and vertical distance (D_{PtO}) of absorbed O to Pt top layer for atomic oxygen adsorbed on hcp site, and the vertical distance between top and second Pt layer(D_{PtPt}), at the transition state (TS) for migration to the subsurface, and in subsurface tetrahedral site with total coverage of 0.25 ML and 0.50 ML.

Coverage/ ML		0.00/0.25	0.25/0.50
Hcp	R_{PtPt}/ Å	2.875	2.794
	D_{PtO}/ Å	1.215	1.293
	D_{PtPt}/ Å	2.410	2.362
	R_{PtPt}/ Å	3.208	3.156
TS	D_{PtO}/ Å	~ 0	~ 0
	D_{PtPt}/ Å	2.611	2.703
Tetra	R_{PtPt}/ Å	3.117	2.859
	D_{PtO}/ Å	-0.781	-1.118
R_{PtPt} change/ hcp to TS		0.333	0.362
R_{PtPt} change/ tetra to TS		0.091	0.297
D_{PtPt} change/ hcp to TS		0.201	0.341

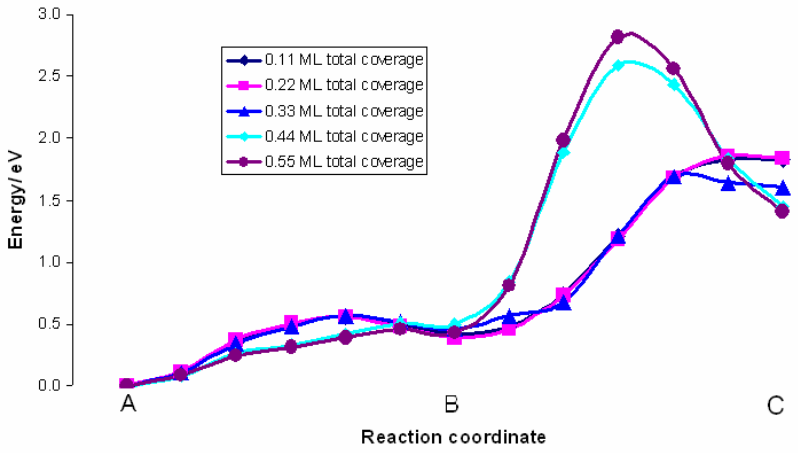

Figure 5.2. Minimum energy paths of oxygen absorption into the Pt(111) subsurface at constant 0.11 ML oxygen subsurface coverage with total oxygen coverage of 0.11, 0.22, 0.33, 0.44 and 0.55 ML. A: fcc hollow site; B: hcp hollow site; C: subsurface tetrahedral site.

Figure 5.2 shows the MEPs for migration of oxygen at *total* coverage of 0.11, 0.22, 0.33, 0.44 ML, and 0.55 ML in all cases yielding 0.11 ML oxygen absorption into the Pt(111) subsurface tetrahedral site. For *total* coverage of 0.11 ML and 0.22 ML, the MEPs and the energy barriers for on-surface oxygen diffusion and absorption into the subsurface are almost identical, this indicates that a low *total* oxygen coverage < 0.22 ML has little effect on the absorption process. Besides, the reverse energy barriers are almost zero indicating that the subsurface oxygen is very unstable at this small coverage though the absorption energy barrier of 1.37 eV from hcp to the subsurface tetrahedral site is smaller than that at the 0.25 ML subsurface oxygen cases shown in Figure 5.1. At *total* coverage of 0.33 ML with 0.22 ML on-surface coverage (Figure 5.2), the reverse energy barrier increased to 0.09 eV with an absorption energy barrier of 1.23 eV from hcp to the subsurface, a little smaller than that at 0.11 ML and 0.22 ML. At 0.44 ML *total* atomic oxygen coverage with 0.33 ML on-surface, the absorption energy barrier from hcp to subsurface increased to 2.10 eV and the reverse energy barrier was 1.14 eV.

At *total* oxygen coverage of 0.55 ML with 0.44 ML oxygen on surface, the absorption energy barrier from *hcp* to the subsurface tetrahedral site increased to 2.36 eV and the reverse energy barrier increased to 1.40 eV. Therefore, the increase of the reverse energy barrier when the on-surface coverage increases suggests that increasing the surface oxygen coverage can stabilize the subsurface oxygen mainly due to the increased repulsion between surface oxygen atoms. The relaxed geometries with subsurface oxygen shown in Figure 5.3 and the D_{PtO} values (defined as the average vertical distance between the subsurface oxygen and the top layer Pt atoms coordinating with subsurface oxygen) shown in Table 5.3 reveal that the subsurface oxygen atoms lodge deeper away from the top Pt layer with the coverage increasing. Such deeper subsurface oxygen atom is more stable based on the above thermodynamic and kinetic analysis. The increased energy barriers for the forward and reverse diffusion reaction at higher *total* coverage and 0.11 ML subsurface coverage can be explained with the same arguments used when discussing the 0.25ML subsurface coverage (Figure 5.1). As the total coverage increases a large lattice deformation is induced as observed in Figure 5.3 and table 5.3. Thus, more energy is required to produce the larger lattice deformation necessary for the diffusion of oxygen into the subsurface. Also, as the total coverage increases, the subsurface oxygen lodges deeper into the subsurface making the reverse process more difficult, and consequently stabilizing the subsurface oxygen.

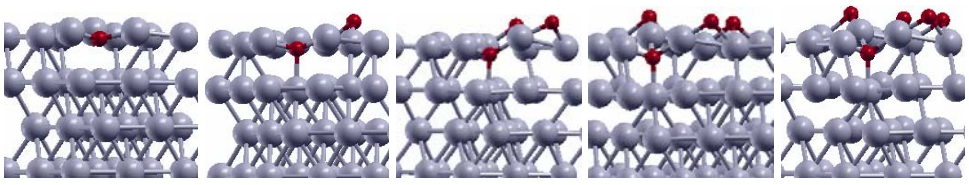

a b c d e

Figure 5.3. Relaxed geometries for 0.11 ML oxygen in the subsurface at various total oxygen coverage. a) 0.11 ML, b) 0.22 ML, c) 0.33 ML, d) 0.44 ML, e) 0.55ML.

Table 5.3: DFT calculated Pt-O bond distance (R_{PtO}) between subsurface absorbed O and Pt atoms in the top layer, Pt-Pt bond length (R_{PtPt}) at the hcp site in the top layer which coordinates with absorbed O, and vertical distance (D_{PtO}) of absorbed O to Pt top layer for atomic oxygen adsorbed on hcp site, at the transition state (TS) of absorption, and in the subsurface tetrahedral site with total coverage of 0.11, 0.22, 0.33, 0.44, and 0.55 ML.

Coverage/ ML		0.00/0.11	0.11/0.22	0.22/0.33	0.33/0.44	0.44/0.55
hcp	R_{PtPt}/ Å	2.921	2.884	2.795	2.751	2.721
	D_{PtO}/ Å	1.177	1.222	1.307	1.351	1.379
TS	R_{PtPt}/ Å	3.369	3.355	3.321	3.288	3.261
	D_{PtO}/ Å	~ 0	~ 0	~ 0	~ 0	~ 0
Tetra	R_{PtPt}/ Å	3.349	3.316	3.237	3.084	3.022
	D_{PtO}/ Å	-0.378	-0.452	-0.592	-0.860	-0.873
R_{PtPt} change/hcp to TS		0.448	0.471	0.526	0.537	0.540
R_{PtPt} change/tetra to TS		0.020	0.039	0.084	0.204	0.239

*surface coverage /total coverage

Can we relate the above discussion to some experimental evidence about the Pt dissolution process? Values of the platinum dissolved equilibrium concentration were determined in an electrochemical experiment when the cell potential was set at a given value between 0.65 V to 1.1 V (in the oxide formation region) at constant potential conditions, and compared to those obtained by cycling between platinum oxide formation and reduction voltages[53]. The results clearly indicate[53] that platinum dissolution is accelerated by three to four orders of magnitude upon cycling compared to holding the potential at a fixed value. Thus, assuming that the atomic oxygen inside the subsurface is a critical or even a controlling step for Pt dissolution, the much smaller measured dissolution values in this potential range at constant voltage can be explained due to the difficulty of forming stable subsurface atomic oxygen at fixed surface

coverage, especially at relatively low surface coverage, which corresponds to potentials at the onset of oxide growth (approximately between 0.6 and 1 V). As mentioned in the Introduction, the higher dissolution rates measured by cycling rather than static potential condition has been explained by the formation and disruption of place-exchanged oxide film leading to mobile platinum species[53,60]. Our investigation shows that at low oxygen coverage -corresponding to low potential- the energy barrier of atomic oxygen absorption into the subsurface was much lower, indicating that at these conditions it is comparatively easier for atomic oxygen to migrate into the subsurface. With increasing coverage corresponding to increasing potential, the higher surface coverage stabilizes the absorbed subsurface atomic oxygen. Therefore, in the potential cycling process more atomic oxygen could be absorbed into the subsurface at lower potential corresponding to lower coverage, then higher coverage (higher potential) could stabilize these subsurface oxygen atoms, thus explaining the higher dissolution rate in cycling potential than in static potential experiments based on the hypothesis of subsurface oxygen absorption being the controlling step for platinum dissolution.

5.2. Effect of OH Adsorbate on the Absorption Process. During the oxygen reduction process there are different oxygen reduction intermediates on the cathode catalyst surface such as OH and OOH. Here we present the effects of adsorbed OH on the oxygen absorption into the Pt(111) subsurface. Table 5.4 shows the energy difference (ΔE, defined in the previous section) comparing the effect of on-surface O and OH as a function of total coverage at fixed 0.25 ML subsurface coverage. ΔE decreases with the on-surface OH coverage increasing, indicating that higher OH on-surface coverage can also stabilize subsurface oxygen. Table 5.4 reveals that from 0.25 ML to 0.50 ML surface coverage the ΔEs with on-surface oxygen are much smaller than those with OH on the surface; thus at on-surface coverage $\leq$ 0.50 ML, on-surface oxygen can stabilize the subsurface oxygen more than OH can. However, at OH on-surface coverage of 0.75ML ΔE becomes -1.41 eV, much more negative than the value of -0.35 eV obtained with the same coverage of on-surface oxygen, therefore at higher total

coverage the OH intermediate can stabilize the subsurface oxygen much more than surface oxygen from an energetic point of view.

Table 5.4: Energy difference (ΔE, in eV) at constant total coverage between systems with and without subsurface oxygen with OH adsorbed on surface. The on-surface coverage is indicated as "on-surface coverage/total coverage", with the second row corresponding to on-surface OH and the third row to on-surface oxygen, in both cases at 0.25 ML subsurface oxygen.

Coverage*, ML		0.00/0.25	0.25/0.50	0.50/0.75	0.75/1.0
OH	ΔE/ eV	1.99	1.48	1.17	-1.41
O		1.99	0.79	0.13	-0.35

*surface coverage /total coverage

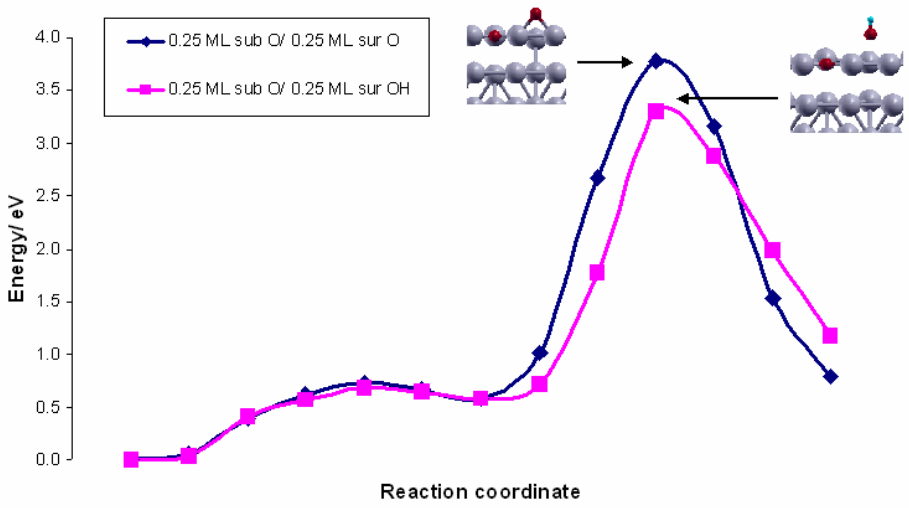

Figure 5.4. Minimum energy paths for 0.25 ML atomic oxygen absorption into Pt(111) subsurface at total coverage of 0.50 ML (0.25 ML on surface, 0.25 ML subsurface). Blue stands for on-surface oxygen coverage and pink stands for on-surface OH coverage.

Figure 5.4 shows the MEP with 0.25 ML OH on-surface adsorption and 0.25 ML subsurface oxygen (total coverage OH + O of 0.50 ML), and the MEP corresponding to the same total coverage where O is adsorbed on the surface instead of OH. Both MEPs represent the same phenomena: atomic oxygen diffusion from fcc to hcp on the surface, then oxygen migration into the subsurface. At 0.25 ML OH adsorbate with total coverage 0.50 ML there are no significant effects on the surface diffusion from fcc to hcp compared with total 0.50 ML oxygen coverage. For the absorption from hcp into the subsurface the energy barrier with OH surface coverage is 2.71 eV which is smaller than the energy barrier of 3.18 eV with the same O surface coverage, thus the presence of OH on the surface decreases the energy barrier for O migration from hcp to the subsurface compared to the same on-surface oxygen coverage. Both transition states have the atomic oxygen in the hcp site (Figure 5.4), but the vertical distance of OH to the top layer is 2.05 Å which is larger than that of the on-surface O (1.52 Å) in the transition state configuration. The reverse energy barrier with on-surface OH is 2.12 eV, smaller than 2.98 eV with the same coverage of oxygen on- surface, indicating that on-surface oxygen can stabilize the subsurface oxygen more than on-surface OH at the same subsurface coverage of 0.25 ML from a kinetic point of view.

5.3. Water Solution Effects on the Absorption Process. One monolayer of water molecules was introduced into the (2×2) super-cell system to investigate the water effects on the 0.25 ML atomic oxygen absorption into the subsurface. Table 5.5 shows the ΔEs for systems with 0.25 ML subsurface oxygen and various values of total coverage, in one case without water (first row) and another with 1ML water above the adsorbed oxygen (second row). The ΔEs in systems with water decrease with the total oxygen coverage increasing and at total oxygen coverage of 1.00 ML the absorption process becomes energetically favorable with negative ΔE of -0.64 eV. The ΔE values in the systems with water are a little bit smaller than those without water at each specific coverage value, which suggests that water solution can stabilize the subsurface oxygen to some extent. However, at *total* coverage $\leq$ 0.75ML the stabilization effect of water

solution on subsurface oxygen is small as observed by comparing the ΔEs at the same coverage obtained with and without water, for example, at *total* coverage of 0.75 ML the ΔE with water is 0.12 eV, only 0.01 eV smaller than that without water (0.13 eV). At *total* oxygen coverage of 1.00 ML the water solution stabilization effect becomes larger based on the ΔE obtained with water (-0.64 eV), around 0.3 eV more negative than that without water (-0.35 eV), which indicates that the water solution stabilization effect on subsurface oxygen becomes clear above certain high surface atomic oxygen coverage probably due to the increased interactions between surface adsorption oxygen atoms and water molecules.

Figure 5.5 shows the interaction between adsorbed oxygen and water. The O..H bond lengths between adsorbed atomic oxygen and water hydrogen at both fcc and hcp hollow sites are 1.97 Å which is longer than the average H-bond length in liquid water (1.80 Å for a linear H-bond[117]), indicating that the interaction is slightly weaker than the interaction among water molecules. The corresponding OH..O angles in the fcc and bridge sites are 153.62 and 166.23^{o}, respectively. At the bridge site, transition state for O surface diffusion from fcc to hcp, the O..H bond length is 2.05 Å, also longer than the linear O..H bond length among water molecules, and the OH..O angle is 174.57^{o}. Once the atomic oxygen is absorbed into subsurface, the water layer becomes flat, with the molecular dipole moment parallel to the surface.

Table 5.5: Energy difference (ΔE, in eV) at constant total coverage between systems with and without subsurface oxygen with water in system. The on-surface coverage is indicated as "on-surface coverage/total coverage" for systems without water (2nd row) and with water (3rd row) at 0.25 ML subsurface oxygen.

0.25 ML atomic oxygen in subsurface:				
Coverage*, ML	0.00/0.25	0.25/0.50	0.50/0.75	0.75/1.00
ΔE/ eV	1.99	0.79	0.13	-0.35
ΔE/ eV/ H2O	2.03	0.75	0.12	-0.64

*surface coverage /total coverage

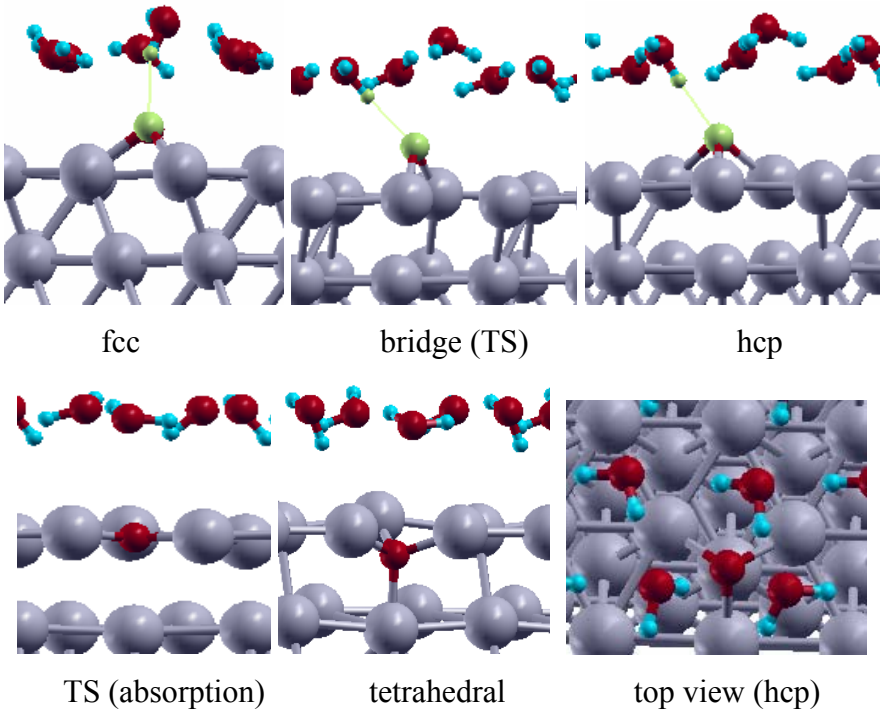

Figure 5.5. Water structure over surface containing 0.25 ML adsorbed oxygen. Top: fcc, bridge (transition state), hcp. Bottom: transition state for O diffusing to the subsurface, tetrahedral site, and top view of the water monolayer over 0.25ML O on the hcp site.

Figure 5.6 shows the water effects on the MEP for atomic oxygen absorption into the subsurface at 0.25ML oxygen coverage. As in the process without water, the atomic oxygen diffuses from fcc hollow site to hcp hollow site, and then it migrates into the subsurface tetrahedral site. The energy barrier of surface diffusion from fcc site to hcp and the corresponding reverse energy barrier are almost the same with water and without water, indicating that the water solution has few effects on the atomic oxygen surface diffusion. However, the water solution can stabilize the atomic oxygen along the surface diffusion path as observed by comparing the energies at the corresponding reaction coordinates except at the bridge (transition state) site. For the absorption from hcp into

the subsurface tetrahedral site, both the absorption energy barrier and the reverse energy barrier of absorption with water in system are very similar to those without water; thus the water solution does not have significant effects on the absorption process, although again we observe an energetically stabilizing effect of water on the migration of O to the subsurface, except at the transition state. Therefore, at low subsurface coverage of 0.25 ML the water solution has small impact on the diffusion of the on-surface adsorbed atomic oxygen and on the absorption process from hcp to the tetrahedral subsurface site.

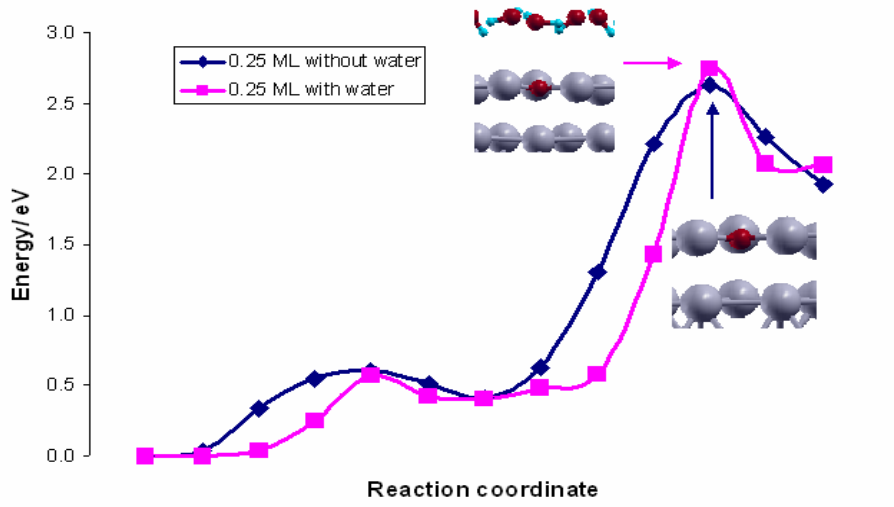

Figure 5.6. Minimum energy paths for 0.25 ML oxygen absorption into Pt(111) subsurface at total coverage of 0.25ML with 1ML of water over the adsorbed on-surface oxygen and without water in the system.

5.4. Summary. Spin polarized DFT calculations show that the increasing surface coverage of atomic oxygen can stabilize from an energetic and kinetic point of view the subsurface atomic oxygen at both 0.25 ML and 0.11 ML subsurface oxygen coverage. Similar on-surface oxygen coverage has different stabilizing effects on different coverage of subsurface oxygen, with higher subsurface coverage (0.25 ML) inducing higher thermodynamic stability. With the oxygen on-surface coverage increasing the

energy barrier of absorption from hcp to the subsurface tetrahedral site increased and the corresponding reverse energy barrier also increased at 0.25ML subsurface oxygen. At 0.11 ML subsurface atomic oxygen, oxygen on-surface coverage $\leq$ 0.22 ML has little effect on the absorption energy barrier, with such barrier and the corresponding reverse energy barrier increasing clearly at surface coverage $\geq$ 0.33 ML. The OH adsorbate has similar effects on the atomic oxygen absorption process as the adsorbed on-surface atomic oxygen. Water solution has relatively small effects on the atomic oxygen absorption process from both energetic and kinetic points of view; although a stabilization effect is detected.

Analyses of the calculated minimum energy paths for migration of oxygen from the surface into the subsurface of Pt(111) provide a plausible explanation to the experimentally detected difference in measured amounts of dissolved platinum in electrochemical experiments using platinum electrodes in acid medium at constant voltage and those performed by cycling potentials. The explanation is based on the hypothesis that oxygen diffusion into the subsurface is an important step in the formation of the surface oxide, and of the subsequent platinum dissolution. In the region of oxide formation, and at constant potential (constant surface oxygen coverage), the calculated MEPs show that it is difficult for oxygen to penetrate to the subsurface. Instead, by cycling the potentials, at low potentials (low surface coverage) oxygen may go into the subsurface and as potential increases surface oxygen coverage increases and stabilizes the subsurface oxygen. Thus, it would be more likely for the subsurface oxygen to become stable as the oxygen coverage increases than if it is held constant.

CHAPTER VI

ATOMIC OXYGEN ABSORPTION INTO PT-BASED ALLOY(111) SUBSURFACES

In previous chapters we discussed the atomic oxygen absorption process into most energetically stable platinum subsurface sites and the chemical environmental effects on the absorption process. In this chapter we present the atomic oxygen absorption in the (111) subsurfaces of Pt-based alloys with various compositions from kinetic and thermodynamic points of view and analyze the alloyed specie effects on the absorption. Transition metals of Co, Ni, Ru, Rh, Pd, and Ir are the alloyed species. The 2×2 unit super-cell and total atomic oxygen coverage of 0.25 ML were employed in the study.

6.1. Atomic Oxygen Absorption into (111) Subsurfaces of Pt-based Bimetallic Alloys (PtX, X= Co, Ni, Ru, Rh, Pd, and Ir). The calculated lattice constants of Pt-X alloys are listed in Table 6.1. PtX alloys have smaller lattice constants than that of pure Pt, when the alloys involve transition metals with smaller lattice constants. For the PtX alloys there are various different fcc and hcp three fold sites. Here we refer as fcc-1 and hcp-1 to fcc and hcp sites respectively which comprise two Pt atoms and one alloyed atom, and fcc-2 and hcp-2 to fcc and hcp sites which comprise one Pt atom and two alloyed atoms. For the subsurface tetrahedral site underneath the hcp site, which is the most energetically stable subsurface site for atomic oxygen[118], there are two different types of the sites. We define tetra-1 and tetra-2 to the subsurface tetrahedral sites which are comprised of three Pt atoms and one alloyed atom beneath the hcp-1 site, and one Pt atom and three alloyed atoms beneath hcp-2 site, respectively (Figure 6.1). The binding energy (E_b) of atomic oxygen adsorbed on the fcc and hcp hollow sites and the absorption energy (E_{ab}) of atomic oxygen absorption into the subsurface tetrahedral sites were calculated by the equation: $E = E_{OPtX} - E_{PtX} - E_{O,}$ here, E_{OPtX} is the energy of oxygen adsorption on Pt surface or energy of oxygen absorption in the Pt subsurface; E_{PtX} is the energy of clean Pt-X alloy surfaces; E_O is the energy of an isolated oxygen atom at its ground state.

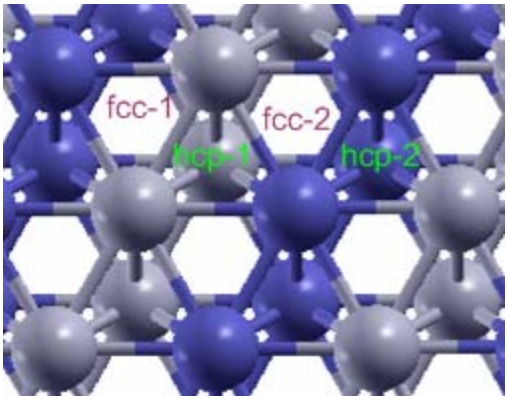

Figure 6.1. fcc-1, fcc-2, hcp-1, and hcp-2 sites on PtX alloy surfaces (in top view). Pt atoms are in grey and alloyed atoms are in blue. Only the top two layers are shown in this figure for better visualization.

Table 6.1: Calculated lattice constants, binding energies (eV) of 0.25 ML atomic oxygen on fcc and hcp hollow sites, and absorption energies (eV) of 0.25 ML inside tetrahedral sites beneath hcp hollow sites of Pt-X alloys (X=Co, Ni, Ru, Rh, Pd, and Ir).

	Lattice constant	fcc-1 2Pt-1X	fcc-2 1Pt-2X	hcp-1 2Pt-1X	hcp-2 1Pt-2X	tetra-1 3Pt-1X	tetra-2 1Pt-3X
Pt-Co	3.801	-4.97	-5.17	-4.72	-5.13	-0.60	-3.74
Pt-Ni	3.800	-4.95	-4.96	-4.55	-4.95	-0.68	-3.74
Pt-Ru	3.895	-5.00	-5.56	-4.86	-5.51	-2.31	-3.39
Pt-Rh	3.911	-4.80	-4.99	-4.49	-4.84	-2.16	-2.90
Pt-Pd	3.960	-4.72	-4.40	-4.37	-4.34	-2.63	-2.61
Pt-Ir	3.926	-4.58	-4.94	-4.35	-4.77	-2.15	-2.55
Pt	3.977	-4.61		-4.21		-2.66	

Table 6.1 shows the binding energies (E_bs) on various fcc and hcp sites and absorption energies (E_{ab}s) inside two different subsurface sites. The fcc-2 sites are the most energetically stable sites for the atomic oxygen adsorption on Pt-X alloy surfaces except in the PtPd case, for example, the binding energy of 4.94 eV on fcc-2 is larger than those on other sites in PtIr, whereas, the binding energy of 4.72 eV on fcc-1 site is larger than those in other sites in the PtPd case. Comparing the two hcp sites, we found that hcp-2 sites are energetically more favorable than those in hcp-1 sites in most of the studied alloys except in the PtPd alloy in which hcp-1 and hcp-2 have very similar binding energies. Both the fcc-2 and hcp-2 are composed of one Pt atom and two alloyed metal atoms. Table 6.2 shows the metal-O bond lengths of atomic oxygen on fcc-2 and hcp-2 sites. From the data we can find the bond lengths of Pt-O are longer than those of the alloyed metal-O (R_{XO}) except in the Pt-Pd case, which could explain why in the PtPd alloy the most favorable site is fcc-1 instead of fcc-2: more Pt atoms in fcc-1 than in fcc-2 and the R_{PtO} distance is shorter than R_{PdO}. Comparing the binding energies on fcc-2 sites of alloys (fcc-1 of PtPd) with that of pure platinum, the binding energies are more negative on alloy surfaces than those on a pure platinum surface, indicating that certain alloy species such as Co, Ni, Ru, Rh, and Ir can thermodynamically favor the atomic oxygen adsorption on Pt-based alloy metallic surfaces. Table 6.1 also shows that the absorption energy of tetra-2 is more negative than that of tetra-1 except for PtPd in which tetra-1 and tetra-2 have very similar absorption energies, indicating that tetra-2 is the most energetically stable subsurface site in most cases. Therefore, the atomic oxygen inside tetra-2 sites (tetra-1 of PtPd) was considered the final state in the following absorption process investigations.

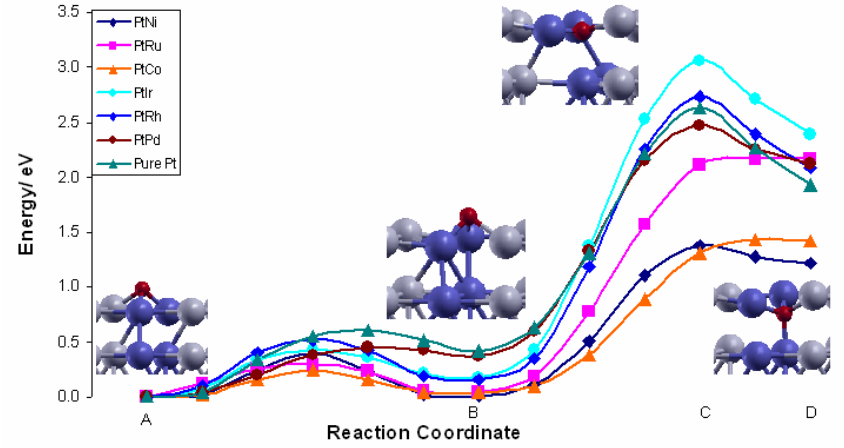

(a)

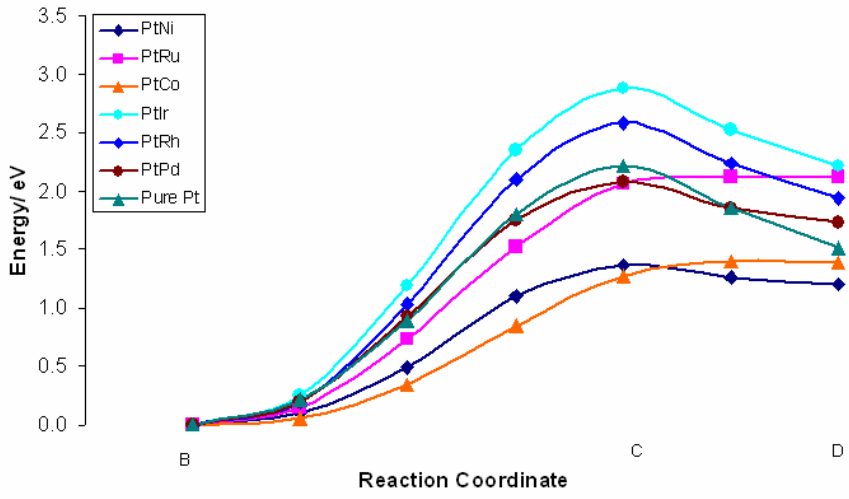

(b)

Figure 6.2. Minimum energy path of atomic oxygen diffusion from the fcc-2 surface site to the subsurface tetrahedral/tetra-2 site in PtX(111) surface cell at the atomic oxygen coverage of 0.25 ML. (a) fcc-2 to hcp-2 into tetra-2 (fcc-1 to hcp-1 into tetra-1 in PtPd); (b) hcp-2 into tetra-2 (hcp-1 into tetra-1 in PtPd). A: O adsorbed on fcc-2; B: O adsorbed on hcp-2; C: O in hcp-2 site; D: O absorbed inside tetra-2. Pt atoms are in grey, alloyed atoms are in blue, O atom is in red.

Table 6.2: Pt-O and X-O bond lengths (R_{PtO}/Å and R_{XO}/ Å respectively) of atomic oxygen atom adsorbed on fcc-2 and hcp-2 sites of Pt-X alloys.

		Pt-Co	Pt-Ni	Pt-Ru	Pt-Rh	Pt-Pd*	Pt-Ir
fcc-2	R_{PtO}	2.082	2.046	2.070	2.054	2.022	2.084
	R_{XO}	1.862	1.853	1.987	2.004	2.077	2.029
hcp-2	R_{PtO}	2.072	2.033	2.105	2.048	2.008	2.102
	R_{XO}	1.876	1.859	1.984	1.997	2.144	2.009

*In Pt-Pd case, the Pt-O and X-O correspond to adsorption on fcc-1 and hcp-1.

Figure 6.2a shows the minimum energy paths for atomic oxygen diffusion from the most energetically stable surface adsorption sites to the most energetically stable subsurface sites. Atomic oxygen diffuses from fcc sites (A in figure 2a) to hcp sites (B in Figure 6.2a) across bridge sites, then the atomic oxygen migrates into subsurface sites (D in Figure 6.2). For the surface diffusion, the diffusion energy barriers (0.25 eV, 0.39 eV, 0.30 eV, 0.52 eV, 0.45 eV, and 0.43 eV on PtCo, PtNi, PtRu, PtRh, PtPd, and PtIr respectively) on alloys are smaller than that of 0.60 eV on pure Pt and the corresponding reverse energy barriers (0.21 eV, 0.38 eV, 0.20 eV, 0.28 eV, 0.08 eV, and 0.19 respectively) are similar to that of 0.20 eV except on PtPd, indicating that the atomic oxygen diffusion on Pt-based alloys with 50% alloyed metals (Co, Ni, Ru, Rh, Pd, Ir) (111) is kinetically easier than on pure platinum surfaces. To prevent atomic oxygen absorption into the subsurface, higher absorption energy barriers and lower reverse absorption energy barriers than those of pure Pt can achieve this goal kinetically, and the introduction of a second transition metal species could be an effective way to prevent atomic oxygen absorption into the subsurface. Since the energy barrier of absorption into the subsurface is much higher than that of the atomic oxygen surface diffusion on the surface[118], here we present the absorption starting from the hcp-2 to the tetra-2 (most energetically stable subsurface sites) subsurface site in PtX alloy cases and compare the second alloyed specie effects on the absorption. Figure 6.2b shows the minimum energy

path of atomic oxygen absorption into the subsurface from the hcp-2 to tetra-2 in various Pt-X alloys (hcp-1 to tetra-1 in PtPd). The transition state is the atomic oxygen in the hcp-2 site. The absorption energy barriers in PtIr (2.88 eV) and PtRh (2.58 eV) are higher than that in pure Pt (2.22 eV) (Figure 6.2b, from hcp-2 to tetra-2), indicating that the introduction of Ir and Rh can increase the absorption energy barrier, which is helpful to kinetically prevent the atomic oxygen absorption into the subsurface. The reverse absorption energy barriers of PtIr and PtRh are 0.66 eV and 0.64 eV respectively which are close to 0.70 eV of pure Pt, indicating that the introduction of 50% Ir or Rh did not significantly decrease the reverse energy barrier. The absorption energy barriers of PtCo, PtRu, PtNi, and PtPd are 1.40 eV, 2.12 eV, 1.36 eV, and 2.07 eV respectively, which are lower than 2.22 eV pure Pt. However, the reverse absorption energy barriers of Pt-Co, Pt-Ru, Pt-Ni, and Pt-Pd are 0.01 eV, 0.00 eV, 0.16 eV, and 0.34 eV lower than 0.70 eV of pure Pt, indicating that the introduction of 50% Co, Ru, Ni, and Pd decrease the energetic stabilities of subsurface oxygen. Especially in the Pt-Co and Pt-Ru cases, the reverse energy barriers are close to zero, indicating that kinetically the atomic oxygen almost cannot exist inside Pt-Co and Pt-Ru subsurfaces, which also can prevent the atomic oxygen absorption into the subsurface due to kinetically unstable subsurface oxygen.

In a previous chapter we discovered that the absorption energy barrier increased with the coverage increasing due to the higher oxygen repulsion and higher geometric deformation at high oxygen coverage. The geometric deformations of PtX alloys during absorption process are listed in Table B-2 of the Appendix. However, different from pure Pt surfaces, the deformations of alloys do not give out a clear trend related to the various absorption energy barriers due to introduction of different alloyed metals. Table 6.3 shows the charge changes (ΔC) of atomic oxygen during the absorption process in PtX alloys, which were calculated by Bader Charge Density Analysis method[119]. Atomic oxygen becomes more charged when going from the hcp-2 to the TS state in PtIr and PtRh alloys (Table 6.3) with higher absorption energy barriers than other alloys (Figure 6.2), indicating that oxygen withdrawing more electron density from the metal atoms

contributes to higher absorption energy barriers. However, other factors such as the high extent of geometric deformation also contributes to increase the absorption energy barriers, therefore the energy barrier does not increase monotonically with charge transfer increasing. For the reverse process from tetra-2 to TS, the charge changes of atomic oxygen are smaller than the corresponding absorption from hcp-2 to TS. Clear negative charges increasing from tetra-2 to TS in PtIr and pure Pt contribute to higher reverse energy barriers (Table 6.3 and Figure 6.2).

Table 6.3: Atomic oxygen charge at hcp site, in hcp site, and inside subsurface tetrahedral site and charge changes (ΔC) of atomic oxygen during absorption from hcp-2 to tetra-2. Negative or positive ΔC means oxygen obtains or losses electron density.

	PtCo	PtNi	PtRu	PtRh	PtPd*	PtIr	Pt
hcp-2	-0.9203	-0.8928	-0.9194	-0.7982	-0.7792	-0.8498	-0.7356
TS	-1.0036	-1.0320	-1.0645	-1.0567	-0.9070	-1.1630	-1.0672
tetra-2	-1.0669	-1.0581	-1.0569	-1.0084	-0.9217	-1.0485	-0.9538
$\Delta C_{hcp\text{-}TS}$	-0.0773	-0.1392	-0.1451	-0.2585	-0.1278	-0.3132	-0.3326
$\Delta C_{tetra\text{-}TS}$	0.0633	0.0261	-0.0076	-0.0483	0.0147	-0.1145	-0.1034

*In Pt-Pd case, hcp-1 and tetra-1 instead of hcp-2 and tetra-2.

6.2. Atomic Oxygen Absorption into (111) Subsurfaces of Pt_3X (X= Co, Ru, Rh, and Ir). According to the above investigation, the introduction of Ir and Rh can increase the energy barrier of atomic oxygen absorption into the subsurface and the introduction of Co and Ru can decrease the reverse energy barrier of atomic oxygen absorption. Both increased absorption energy barrier and decreased reverse absorption energy barrier could kinetically inhibit the atomic oxygen absorption into subsurface. We also investigated Pt-based bimetallic alloys with 3:1 ratio to compare the absorption behavior with the above corresponding 1:1 ratio alloys. The calculated lattice constants of Pt_3Co,

Pt_3Ru, Pt_3Rh, and Pt_3Ir are 3.927, 3.950, 3.971, and 3.969 respectively and the corresponding available experimental lattice constants of Pt_3Co and Pt_3Ir are 3.85[120], and 3.90[121], indicating that our calculated results are close to the experimental results. There are different types of three fold hollow sites (fcc and hcp) due to the different compositions (Figure 6.3). Here we define fcc-I to fcc sites comprising two Pt atoms and one alloyed metal atom; fcc-II to fcc sites composed of three Pt atoms; hcp-I to hcp sites above alloyed metal atom comprising two Pt atoms and one alloyed metal atom; hcp-II to hcp sites above Pt atom consisting of three Pt atoms; hcp-III to hcp sites above Pt atoms composed of two Pt atoms and one alloyed metal atom. Also there are three types of tetrahedral subsurface sites which are defined by their compositions: tetra-I (2 Pt atoms and 2 X atoms) beneath hcp-I; tetra-II (4 Pt atoms) beneath hcp-II; and tetra-III (3 Pt atoms and 1 X atom) beneath hcp-III. Table 6.4 lists the binding energies (E_b) of atomic oxygen at 0.25 ML coverage on fcc and hcp sites and absorption energies (E_{ab}) of atomic oxygen absorption inside subsurface tetrahedral sites, which are calculated by $E = E_{OPt3X} - E_{Pt3X} - E_O$. The fcc-I (2Pt + X) sites are the most energetically stable sites for atomic oxygen adsorption on the catalyst surface in all four Pt alloys according to the more negative binding energies (Table 6.4). Adsorption on hcp-I and hcp-III (2Pt+X) sites have similar binding energies, more negative than those on the hcp-II (3Pt) site. Compared with pure Pt, the introduction of a second species (Co, Ru, Rh, and Ir) in Pt_3X also increased the binding energies compared to pure Pt (fcc-I more negative than Pt fcc, hcp-I more negative than Pt hcp, Table 6.4). According to the absorption energies in Table 6.4, the most energetically stable subsurface site is the tetra-I comprising two Pt atoms and two alloyed metal atoms beneath the hcp-I site.

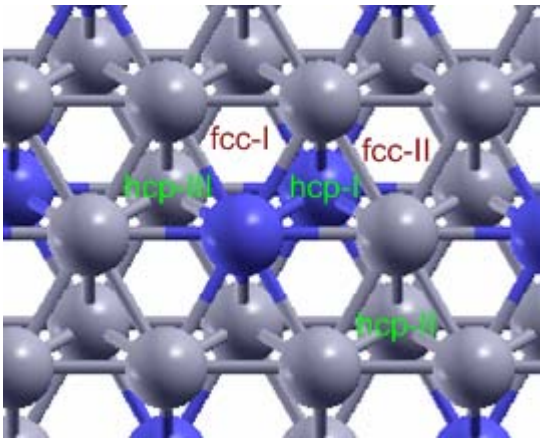

Figure 6.3. fcc-I, fcc-II, hcp-I, hcp-II, and hcp-III sites on Pt_3X alloy surface (in top view). Pt atoms are in grey and alloyed atoms are in blue. Only the top two layers are shown in this figure for better visualization.

Table 6.4: Calculated binding energies (eV) of 0.25 ML atomic oxygen on fcc and hcp hollow sites, and absorption energies (eV)of 0.25 ML inside tetrahedral sites beneath hcp hollow sites of Pt_3X alloys (X=Co, Ru, Rh, and Ir).

	fcc-I 2Pt-1X	fcc-II 3Pt	hcp-I 2Pt-1X	hcp-II 3Pt	hcp-III 2Pt-1X	tetra-I 2Pt-2X	tetra-II 4Pt	tetra-III 3Pt-1X
Pt_3Co	-4.97	-4.47	-4.64	-4.17	-4.65	-3.48	-1.73	-2.89
Pt_3Ru	-5.15	-4.23	-4.78	-3.96	-4.92	-3.11	-2.05	-2.75
Pt_3Rh	-4.87	-4.49	-4.50	-4.14	-4.51	-3.12	-2.44	-2.76
Pt_3Ir	-4.84	-4.23	-4.44	-3.91	-4.58	-2.82	-2.22	-2.55
Pt	-4.61		-4.21			-2.66		

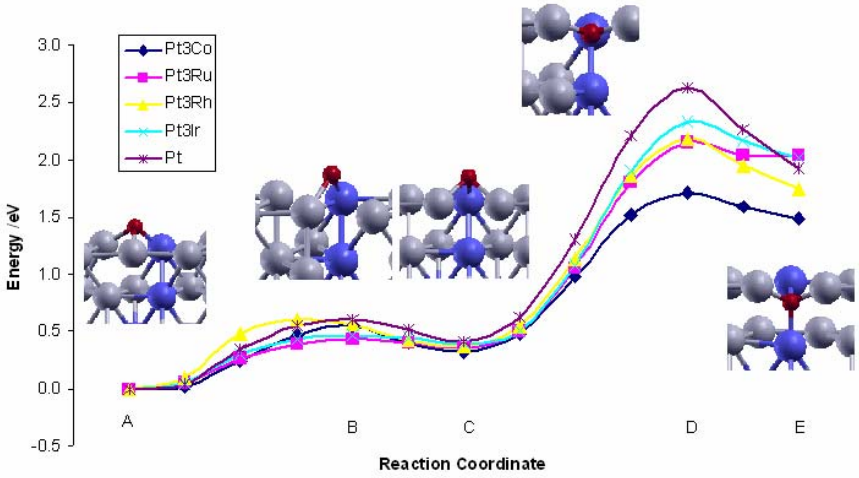

Figure 6.4. Minimum energy path of atomic oxygen diffusion from the fcc-I surface site to the subsurface tetrahedral/tetra-I site in $Pt_3X(111)$ surface cell at the atomic oxygen coverage of 0.25 ML. A: O adsorbed on fcc-I; B: O adsorbed on bridge site; C: O adsorbed on hcp-I; D: O in hcp-I site; E: O absorbed inside tetra-I. Pt in grey, alloyed atom in blue, O in red.

Figure 6.4 shows the minimum energy path of the atomic oxygen absorption into the subsurface site from the fcc-I (most energetically stable on-surface adsorption site) to the most energetically stable tetra-I subsurface site. The atomic oxygen diffused from the fcc-I site (A, Figure 6.4) to hcp-I (C, Figure 6.4) through the bridge site (B, Figure 6.4) which is formed by one Pt atom and one alloyed atom. The energy barriers for the on-surface diffusion are less than 0.60 eV. Then the atomic oxygen migrates into the tetrahedral subsurface site from the hcp-I site into the tetra-I site (E, Figure 6.4) and the transition state is the atomic oxygen in the hcp-I site (D, Figure 6.4). The energy barriers from hcp-I to tetra-I are 1.39 eV, 1.79 eV, 1.81 eV, and 1.94 eV respectively in Pt_3Co, Pt_3Ru, Pt_3Rh, and Pt_3Ir cases, which are lower than 2.22 eV of pure Pt. Compared with the corresponding same component of the PtX alloys in the above section, each of the absorption energy barriers of Pt_3X are smaller than the corresponding of PtX (X=Co, Ru, Rh, and Ir). One reason could be the less negative binding energies on Pt_3X surfaces than

those on PtX surfaces (Table 6.1 and Table 6.4). The reverse absorption energy barriers of Pt_3Co, Pt_3Ru, Pt_3Rh, and Pt_3Ir are 0.23 eV, 0.11 eV, 0.43 eV, and 0.32 eV respectively, smaller than 0.70 eV of pure Pt, indicating that the introduction of 25% alloyed Co, Ru, Rh, and Ir can decrease the energetic stability of subsurface atomic oxygen. Compared with the PtX alloys (X=Co, Ru, Rh, and Ir) the Pt_3Ir and Pt_3Rh have lower absorption energy barriers than PtIr and PtRh, whereas Pt_3Co and Pt_3Ru have higher reverse energy barriers than PtCo and PtRu indicating that the amount of alloyed transition metal also have particular effects on the absorption kinetics.

6.3. Atomic Oxygen Absorption into (111) Subsurfaces of Pt_2IrX (X= Co, Ru). The results in Section 1 of this chapter regarding atomic oxygen absorption into alloy PtX subsurfaces showed that 50% Ir introduction can increase the absorption energy barrier and 50% Co or Ru introduction can decrease the reverse energy barrier of atomic oxygen absorption. In this section we present the atomic oxygen absorption behavior in ternary Pt alloys: Pt_2IrCo and Pt_2IrRu to see the combination effects of two alloyed metals. Similarly to the above two sections, there are different adsorption and absorption sites due to atomic distribution. Here we define that fcc-i and hcp-i are those fcc and hcp sites consisting of one Pt, one Ir and one alloyed atom (X= Co, Ru), fcc-ii and hcp-ii are fcc and hcp sites comprising two Pt atoms and one Ir atom, and fcc-iii and hcp-iii are fcc and hcp sites composed of two Pt atoms and one alloyed atom (X =Co, Ru, Figure 6.5). The absorption subsurface sites tetra-i (two Pt atoms, one Ir atom, and one alloyed atom), tetra-ii (two Pt atoms and two Ir atoms), and tetra-iii (two Pt atoms and two alloyed atoms) are underneath hcp-i, hcp-ii, and hcp-iii sites respectively (Figure 6.5). Table 6.5 shows the binding and absorption energies of atomic oxygen. The tetra-iii (PtPtXX, X= Co, Ru) is the most energetically stable subsurface site for atomic oxygen absorption in Pt_2IrCo and Pt_2IrRu with absorption energies of -2.99 eV and -2.65 eV respectively. fcc-i sites are the most energetically stable sites for atomic surface adsorption according to the binding energies. In Figure 6.6 we present the absorption minimum energy path from fcc-i to tetra-iii. Similarly to previous cases, the atomic oxygen diffuses to hcp-iii (C in Figure 6.6) first, then, migrates into tetra-iii subsurface site (E in Figure 6.6). The

surface diffusion energy barriers of Pt_2IrCo and Pt_2IrRu are 0.89 eV and 0.83 eV respectively, which are higher than the energy barrier of 0.60 eV on a pure platinum surface. The reverse energy barriers for atomic oxygen surface diffusion of Pt_2IrCo and Pt_2IrRu are 0.07 eV and 0.05 eV respectively, much smaller than 0.2 eV of pure platinum, indicating the atomic oxygen adsorption on hcp-iii is kinetically very unstable. The absorption energy barriers from hcp-iii to tetra-iii subsurface site are 1.79 eV, 2.49 eV, and 2.22 eV and the corresponding reverse energy barriers are 0.34 eV, 0.35 eV, and 0.70 eV respectively for Pt_2IrCo, Pt_2IrRu, and pure Pt. The introduction of alloyed Ir and Ru to pure Pt can increase the energy barrier for absorption and decrease the reverse energy barrier, indicating the combination of Ir and Ru can kinetically inhibit the atomic oxygen absorption. Though the absorption barrier from hcp-iii to tetra-iii of Pt_2IrCo is smaller than that of Pt, the energy barriers from fcc-i to tetra-iii are almost the same. The reverse energy barrier of Pt_2IrCo is smaller than that of pure platinum, indicating the subsurface atomic oxygen more unstable than inside a pure Pt subsurface site.

Table 6.5: Calculated binding energies (eV) of 0.25 ML atomic oxygen on fcc and hcp hollow sites, and absorption energies (eV) of 0.25 ML inside tetrahedral sites beneath hcp hollow sites of Pt_2IrX alloys (X= Co, and Ru).

	fcc-i	fcc-ii	fcc-iii	hcp-i	hcp-ii	hcp-iii	tetra-i	tetra-ii	tetra-iii
Pt_2IrCo	-5.28	-4.80	-4.43	-5.07	-4.56	-4.44	-2.78	-1.89	-2.99
Pt_2IrRu	-5.42	-4.58	-4.76	-5.21	-4.30	-4.65	-2.46	-2.05	-2.65

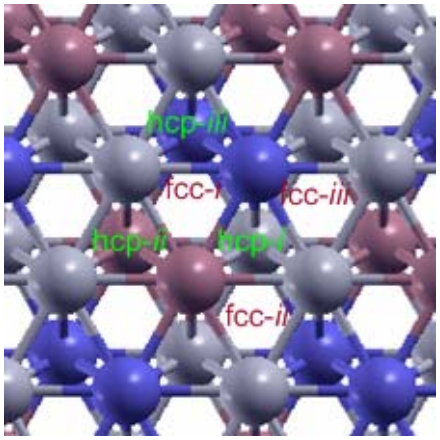

Figure 6.5. fcc-i, fcc-ii, fcc-iii, hcp-i, hcp-ii, and hcp-iii sites on Pt_2IrX alloy (111) surface in top view. Pt atoms are in grey, Ir atoms are in brown, and alloyed atoms (X= Co, Ru) are in blue. Only top two layers are shown in this figure for better visualization.

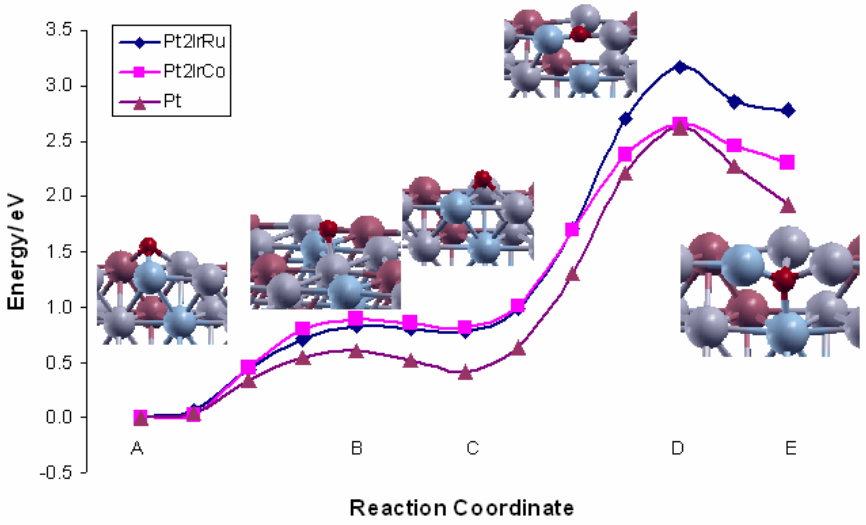

Figure 6.6. Minimum energy path of atomic oxygen diffusion from the fcc-i surface site to the subsurface tetrahedral/tetra-iii site in $Pt_2IrX(111)$ surface cell at the atomic oxygen coverage of 0.25 ML. A: O adsorbed on fcc-i; B: O adsorbed on bridge site; C: O adsorbed on hcp-iii; D: O in hcp-iii site; E: O absorbed inside tetra-iii. Pt in grey, Ir in brown, and alloyed atom in light blue, O in red.

6.4. Atomic Oxygen Absorption into (111) Subsurfaces of Pt_2IrRu with Pt Skin.

The formation of a Pt "skin" has been observed for Pt-based alloy cathode catalysts, which probably results from the alloyed atoms tending to leach out of the alloys during operation in an acidic electrolyte, while the Pt atoms may segregate and rearrange on the cathode surface[122-124]. Pt skin can also be formed by annealing the alloys at high temperature[125] due a strong tendency of the Pt atom to segregate to the surface when Pt is alloyed with most other transition metals[126]. The thickness of the platinum skin on the cathode catalyst remains unknown with certainty, but it is estimated that is less than a few layers[123,125]. Here Pt skins are modeled as a Pt monolayer on the top of Pt_3Ru (111), and Pt_2IrRu(111) substrates with the same lattice constants than those in the corresponding Pt alloys. The three-fold surface adsorption sites for alloys with different compositions are shown in Figure 6.7. Figure 6.7a shows a fcc-a site vertical above an alloyed atom in the third layer and a fcc-b site vertical above a Pt atom in the third layer, while there is an hcp-a site above an alloyed atom in the second layer and an hcp-b site above a Pt atom in the second layer. The tetrahedral subsurface sites of tetra-a (three Pt atoms and one alloyed atom) and tetra-b (four Pt atoms) are beneath hcp-a and hcp-b respectively in Pt_3Ru alloys with Pt skins. For Pt_2IrRu with Pt skin, Figure 6.7b shows three types of fcc sites: fcc-A site vertical above an alloyed Ru atom in the third layer, fcc-B site vertical above an Ir atom in the third layer; fcc-C site vertical above a Pt atom in the third layer, and three types of hcp sites: hcp-A above an alloyed Ru atom in the second layer, hcp-B above an Ir atom in the second layer, and hcp-C site above a Pt atom in the second layer. There are three types of subsurface sites beneath hcp sites (hcp-A, hcp-B, and hcp-C): tetra-A, tetra-B, and tetra-C respectively. The binding energies on Pt skins and absorption energies into subsurface sites of atomic oxygen in Pt_3Ru alloy with Pt skins are listed in Table 6.6. The most energetically stable adsorption sites of Pt skin on Pt_3Ru alloys are fcc-a sites according to their most negative binding energies, indicating that the alloyed atoms in the second layer or third layer have effects on atomic oxygen adsorption (Table 6.6). The most energetically stable subsurface sites are tetra-a

sites based on the most negative absorption energies, indicating that the specific composition of the tetrahedral subsurface sites has an effect on absorption (Figure 7a, Table 6.6). For Pt_2IrRu alloys with Pt skin, the most energetically stable on-surface adsorption sites and subsurface absorption sites are fcc-A and tetra-A (three Pt atoms and one alloyed Ru atom) sites due to their most negative binding energies and absorption energies (Table 6.6).

Table 6.6: Calculated binding energies (eV) of 0.25 ML atomic oxygen on fcc and hcp hollow sites of Pt skins, and absorption energies (eV)of 0.25 ML inside tetrahedral sites beneath hcp hollow sites of Pt_3Ru and Pt_2IrRu with Pt skins respectively.

Pt_2IrRu	fcc-A	fcc-B	fcc-C	hcp-A	hcp-B	hcp-C	tetra-A	tetra-B	tetra-C
	-4.28	-4.20	-4.07	-3.90	-3.81	-3.86	-2.28	-2.08	-1.74
Pt_3Ru	fcc-a	fcc-b	hcp-a	hcp-b	tetra-a	tetra-b			
	-4.36	-4.16	-3.97	-3.86	-2.71	-2.15			

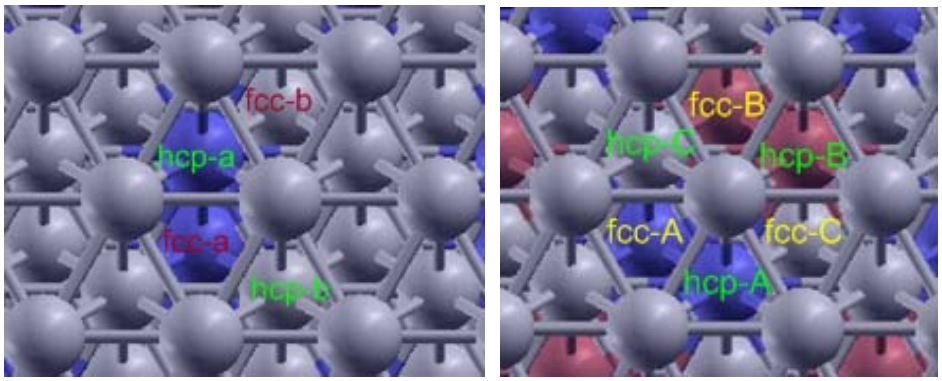

a b

Figure 6.7. Three-fold adsorption sites on Pt skins of Pt_3Ru and Pt_2IrRu. a. fcc-a, fcc-b, hcp-a, and hcp-b on Pt skin of Pt_3Ru; b. fcc-A, fcc-B, fcc-C, hcp-A, hcp-B, hcp-C on Pt skin of Pt_2IrRu. Pt atoms are in grey, Ir atoms are in brown, and Ru atoms are in blue. Only the top three layers are shown in this figure for better visualization.

Minimum energy paths of the atomic oxygen diffusion from the most stable Pt skin sites (fcc-a, fcc-A) to the most stable subsurface sites (tetra-a, tetra-A) are shown in Figure 6.8, in which minimum energy paths of other types of Pt based alloys are also listed for comparison. Similarly to the above Pt alloy cases, in the minimum energy paths the atomic oxygen atom diffuses from fcc-a (fcc-A in Pt_2IrRu with Pt skin) to hcp-a (hcp-B in Pt_2IrRu with Pt skin) first on the Pt skin surface of Pt_3Ru, then atomic oxygen migrates into the subsurface site. The surface diffusion on Pt skins above Pt_3Ru and Pt_2IrRu are very similar to the surface diffusion on pure platinum with similar energy barriers of 0.65 eV, 0.59 eV, and 0.61 eV respectively and reverse energy barriers of 0.15 eV, 0.21 eV, and 0.19 eV respectively. For the absorption process from Pt skin above Pt_3Ru into the subsurface, the energy barrier is 2.30 eV similar to 2.22 eV of pure platinum with a reverse energy barrier of 1.14 eV larger than 0.70 eV of pure platinum, indicating that the atomic oxygen is kinetically more stable in the subsurface of Pt_3Ru with Pt skin. Compared with Pt_3Ru without Pt skin, the absorption energy barrier and the corresponding reverse energy barrier of Pt_3Ru surface with Pt skin are obviously higher due to the presence of the Pt skin. Pt_2IrRu with Pt skin has an absorption energy barrier of 2.96 eV higher than that of pure platinum and its reverse energy barrier of 1.34 eV is also higher than that of pure platinum, indicating the Pt_2IrRu can inhibit the atomic oxygen absorption according to this criterion. Pt_2IrRu alloy without Pt skin has a much smaller reverse absorption energy barrier of 0.39 eV compared to that of Pt_2IrRu with Pt skin, indicating that the existence of the Pt skin layer increases the reverse energy barrier. Table B-4 in appendix B shows that the geometric deformation of R_{PtPt} in hcp-iii site and charge change (ΔC) of atomic oxygen during the absorption process. Both the larger R_{PtPt} deformation and ΔC correspond to larger energy barriers.

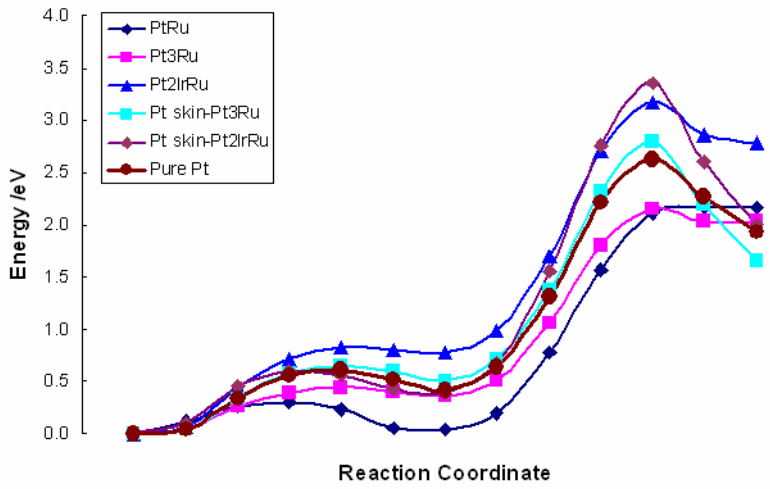

Figure 6.8. Minimum energy path of atomic oxygen diffusion from the most energetically stable surface site to the most stable subsurface tetrahedral site in various Pt based alloys at the atomic oxygen coverage of 0.25 ML. A: O adsorbed on fcc-i; B: O adsorbed on bridge site; C: O adsorbed on hcp-iii; D: O in hcp-iii site; E: O absorbed inside tetra-iii. Pt in grey, Ir in brown, and alloyed atom in light blue, O in red.

6.5. Summary. The introduction of transition metals (Co, Ni, Ru, Rh, Pd, and Ir) into pure platinum can influence the magnitudes of the atomic oxygen absorption energy barrier and reverse energy barrier along the same minimum energy path, in which atomic oxygen diffuses from the most energetically stable fcc site to the hcp site above the most energetically stable subsurface site, then the atomic oxygen migrates into the subsurface site. In the Pt alloys with 50% alloyed transition metals, the introduction of Ir and Rh increased the absorption energy barrier compared with pure platinum which can kinetically inhibit the atomic oxygen absorption and the introduction of Co and Ru can decrease the reverse energy barrier of absorption, which makes the subsurface atomic oxygen more unstable than inside a pure platinum subsurface. The geometric deformation analysis of the alloys during the atomic oxygen absorption could not show a clear relationship between the magnitude of deformation and the absorption energy barrier, though lattice deformation is one reason resulting in the increase of the

absorption energy barrier. The charge analysis of atomic oxygen indicated that the alloys with higher absorption energy barrier or higher reverse energy barrier correspond to more electron density transfer to atomic oxygen during the absorption or during the corresponding reverse process. Comparing the atomic oxygen absorption on Pt_3X alloys with that on PtX alloys, both the alloyed metal species and the amount of alloyed metals in alloys have effects on the atomic oxygen absorption kinetics. Atomic oxygen absorption into the Pt_2IrRu subsurface shows that introduction of two types of alloyed metals such as Ir and Ru can increase the atomic oxygen absorption energy barrier and decrease the reverse energy barrier simultaneously compared with pure platinum, which can inhibit atomic oxygen absorption more effectively. Pt skins on Pt alloys increased both atomic oxygen absorption energy barriers and their corresponding reverse energy barriers due to larger lattice deformation and more electron density transfer to atomic oxygen during the migration process to the subsurface.

CHAPTER VII

CONCLUSIONS AND FUTURE WORK

7.1. Conclusions. Analyses of the calculated ΔGs of possible dissolution reactions involving adsorbed oxygen reduction intermediates in chapter III indicate that five dissolution reactions of oxygen reduction reaction catalysts are thermodynamically favorable. Those cathode catalyst dissolution reactions are electrochemical instead of chemical reactions. The relative stabilities against dissolution of different pure metal cathode catalysts (Pt, Ir, Pd, Rh, Ni, Co) with respect to Pt based on the $\Delta\Delta$G for each dissolution reaction indicate that Ir is the most stable pure catalyst. For alloy cathode catalysts, the introduction of a second metal influences the Pt stability in the alloy catalysts, except for Ni which has little influence on the Pt stability in a PtNi alloy compared with the stability of Pt in pure Pt catalyst. The presence of Ir, Pd, Rh, and Co decreases the stability of Pt in PtIr, PtPd, PtRh and PtCo respectively compared with Pt in a pure Pt cathode catalyst. The relative stabilities of Ir, Pd, Rh, Ni, Co in the corresponding alloy cathode catalysts show similar trends as those of the corresponding pure cathode catalysts, Ir (in Pt-Ir) being the most stable. Comparing the relative stabilities to a given dissolution reaction of Pt and another metal species in the same alloy cathode catalyst, it is found that Ir and Co are more stable than Pt in PtIr and PtCo respectively.

In chapter IV, V, and VI, the spin polarization DFT calculations were employed to study the atomic oxygen absorption into platinum and platinum based ally subsurface process. According to the calculation in chapter IV the most stable adsorption sites on Pt(111) and Pt(100) surface are fcc hollow and bridge respectively. Increasing surface coverage, the binding energies become less negative due to increased oxygen repulsion. The most stable subsurface site of Pt(111) cell is the tetrahedral/tetra-II site underneath a hcp hollow site. The tetrahedral/$tetra_{100}$ site underneath a bridge site is the most stable site in the Pt(100) subsurface at zero surface coverage. Also increasing subsurface coverage the absorption energy becomes less negative and atomic oxygen lodges deeper away from the top layer. Atomic oxygen endothermic absorption into the Pt(111)

subsurface -at low surface coverages- follows this minimum energy path: it migrates from fcc to hcp site with an energy barrier of 0.63 eV where the transition state geometry has the oxygen at a bridge site; then the oxygen atom diffuses into the subsurface tetra-II site from the hcp site with an energy barrier of 2.22 eV and a reverse barrier of 0.70 eV with the atomic oxygen in hcp site as the transition state. For the atomic oxygen endothermic absorption into the Pt(100) surface we found minimum energy paths from hollow to $tetra_{100}$ and from bridge to $tetra_{100}$. The MEP of hollow to $tetra_{100}$ has smaller energy barrier (2.46 eV) than that of bridge to $tetra_{100}$ (4.4 eV). At lower coverage of 0.11ML, the absorption energy barrier on Pt(111) decreases, however, the reverse energy barrier is close to zero, indicating that the subsurface oxygen hardly exists under low surface coverage conditions.

It should be noted that the equilibrium platinum dissolving concentration is very small, in the range of 10^{-9} to 10^{-6} M, measured at various conditions [57]. Therefore, the corrosion controlling elementary step could have very unstable intermediates, also could have high activation energy to produce unstable corrosion intermediates, with small reverse activation energy. If the cathode catalyst would have low activation energy for corrosion, it would not last as the oxygen reduction reaction cathode catalyst in fuel cells. Atomic oxygen penetrating into the subsurface could be the one of elementary steps of platinum cathode corrosion and dissolution; even it could be the controlling step of the whole corrosion process. As indicated in the introduction, we emphasize the need of surface science studies (experimental and computational) on single crystal surfaces which can provide fundamental information about the dissolution mechanism in the same way that binding energies of oxygenated compounds calculated on single crystal surfaces (gas phase studies, no electrode potential incorporated) correlate amazingly well with electrochemical reduction currents.

Spin polarized DFT calculations also show that the increasing surface coverage of atomic oxygen can stabilize from an energetic and kinetic point of view the subsurface atomic oxygen at both 0.25 ML and 0.11 ML subsurface oxygen coverage. Similar on-surface oxygen coverage has different stabilizing effects on different coverage of

subsurface oxygen, with higher subsurface coverage (0.25 ML) inducing higher thermodynamic stability. With the oxygen on-surface coverage increasing the energy barrier of absorption from hcp to the subsurface tetrahedral site increased and the corresponding reverse energy barrier also increased at 0.25ML subsurface oxygen. At 0.11 ML subsurface atomic oxygen, oxygen on-surface coverage $\leq$ 0.22 ML has little effect on the absorption energy barrier, with such barrier and the corresponding reverse energy barrier increasing clearly at surface coverage $\geq$ 0.33 ML. The OH adsorbate has similar effects on the atomic oxygen absorption process as the adsorbed on-surface atomic oxygen. Water solution has relatively small effects on the atomic oxygen absorption process from both energetic and kinetic points of view; although a stabilization effect is detected.

Analyses of the calculated minimum energy paths for migration of oxygen from the surface into the subsurface of Pt(111) provide a plausible explanation to the experimentally detected difference in measured amounts of dissolved platinum in electrochemical experiments using platinum electrodes in acid medium at constant voltage and those performed by cycling potentials. The explanation is based on the hypothesis that oxygen diffusion into the subsurface is an important step in the formation of the surface oxide, and of the subsequent platinum dissolution. In the region of oxide formation, and at constant potential (constant surface oxygen coverage), the calculated MEPs show that it is difficult for oxygen to penetrate to the subsurface. Instead, by cycling the potentials, at low potentials (low surface coverage) oxygen may go into the subsurface and as potential increases surface oxygen coverage increases and stabilizes the subsurface oxygen. Thus, it would be more likely for the subsurface oxygen to become stable as the oxygen coverage increases than if it is held constant.

The introduction of transition metals (Co, Ni, Ru, Rh, Pd, and Ir) into pure platinum can influence the atomic oxygen absorption energy barrier and reverse energy barrier though the minimum energy path are same, in which atomic oxygen diffuses from the most energetically stable fcc site to hcp site above the most energetically stable subsurface site, then the atomic oxygen migrates into subsurface site. In the Pt alloys

with 50% alloyed transition metals, the introduction of Ir and Rh increases the absorption energy barrier compared with pure platinum which can inhibit the atomic oxygen absorption kinetically and introduction of Co and Ru can decrease the reverse energy barrier of absorption, which makes the subsurface atomic oxygen more unstable than inside a pure platinum subsurface. The geometric deformation analysis of the alloys during the atomic oxygen absorption could not show a clear relationship between magnitude of deformation and absorption energy barrier, though the deformation is one reason resulting in the increase of the absorption energy barrier. The charge analysis of atomic oxygen indicated that the alloys with higher absorption energy barrier or higher reverse energy barrier correspond to more electron density transfer to atomic oxygen during the absorption or at the corresponding reverse process. Comparing the atomic oxygen absorption on Pt_3X alloys with that on PtX alloys, both the alloyed metal species and the amount of alloyed metals in alloys have effects on the atomic oxygen absorption kinetics. Atomic oxygen absorption into Pt_2IrRu subsurface shows that introduction of two types of alloyed metals such as Ir and Ru can increase the atomic oxygen absorption energy barrier and decrease the reverse energy barrier simultaneously compared with pure platinum, which can inhibit the atomic oxygen absorption more effectively. Pt skins on Pt alloys increase both atomic oxygen absorption energy barriers and their corresponding reverse energy barriers due to larger lattice deformation and more electron density transfer to atomic oxygen during its migration to the subsurface.

7.2. Future work. Because isolated platinum cations lack part of their electron cloud, therefore, they can not exist as free species in the ionomer or in solution. They are likely to be solvated by water molecules and also may be forming Pt complexes with anions contained in the surrounding polymer membrane. The fluoride and sulfate ions were detected in the outlet water of PEMFC by ion chromatography analysis and the membrane degradation effects were confirmed[45]; in addition significant fluoride release was also detected during fuel cell operation. Therefore, it is suggested to investigate how these possible ligands bind to the cathode catalyst surface, what kind of platinum

complex and what kind of structure of the complex are most favorable to platinum dissolution.

Effects of the surrounding environment on the mechanism of platinum cation dissolution out of the surface into the solution should be investigated, including on-surface coverage, different adsorption species, different subsurface atomic oxygen coverage, water solution, by calculating the energies to dissociate the Pt complex from the surface. The dissociation free energies can tell us the most favorable thermodynamic conditions for the effective separation of the Pt cation complex from the surface and into the solution.

Dissociation elementary processes should be proposed based on the all of previous studies. Energy barriers for each reaction should be calculated for further investigation of this process. The platinum cation complex dissociation pathway and its corresponding energy barrier would be related with experimental reports to provide plausible explanations about the dissolution process at the atomic level.

For many electrochemical processes the metals of interest for catalytic electrodes are usually alloys. The dissolution of alloys above a critical potential as de-alloying is an active area of corrosion study[127,128]. Theoretical study on the potential dependence of alloy dissolution would be important and could be conducted by thermodynamic analysis of the potentials at which the surface alloy dissolution is thermodynamically favorable.

REFERENCES

(1) Mehta, V.; Cooper, J. S. *Journal of Power Sources* **2003**, *114*, 32.

(2) Gamburzev, S.; Appleby, A. J. *Journal of Power Sources* **2002**, *107*, 5.

(3) Cacciola, G.; Antonucci, V.; Freni, S. *Journal of Power Sources* **2001**, *100*, 67.

(4) Chalk, S. G.; Miller, J. F.; Wagner, F. W. *Journal of Power Sources* **2000**, *86*, 40.

(5) Scott, K.; Shukla, A. K. *Reviews in Environmental Science and Bio/Technology* **2004**, *3*, 273.

(6) Costamagna, P.; Srinivasan, S. *Journal of Power Sources* **2001**, *102*, 242.

(7) Alcaide, F.; Cabot, P.-L.; Brillas, E. *Journal of Power Sources* **2006**, *153*, 47.

(8) Girishkumar, G.; Hall, T. D.; Vinodgopal, K.; Kamat, P. V. *Journal of Physical Chemistry B* **2006**, *110*, 107.

(9) Serp, P.; Corrias, M.; Kalck, P. *Applied Catalysis, A: General* **2003**, *253*, 337.

(10) Larminie, J.; Dicks, A. *Fuel Cell Systems Explained*, 1st ed.; Wiley: West sussex, 2002.

(11) Gasteiger, H. A.; Kocha, S. S.; Sompalli, B.; Wagner, F. T. *Applied Catalysis B: Environmental* **2005**, *56*, 9.

(12) Wang, Y.; Balbuena, P. B. *Journal of Physical Chemistry B* **2005**, *109*, 14896.

(13) Xu, Y.; Ruban, A. V.; Mavrikakis, M. *Journal of American Chemical Society* **2004**, *126*, 4717.

(14) Murthi, V. S.; Urian, R. C.; Mukerjee, S. *Journal of Physical Chemistry. B* **2004**, *108*, 11011.

(15) Sidik, R. A.; Anderson, A. B. *Journal of Electroanalytical Chemistry* **2002**, *528*, 69.

(16) Anderson, A. B.; Albu, T. V. *Journal of the Electrochemical Society* **2000**, *147*, 4229.

(17) Panchenko, A.; Koper, M. T. M.; Shubina, T. E.; Mitchell, S. J.; Roduner, E. *Journal of the Electrochemical Society* **2004**, *151*, A2016.

(18) Adzic, R. Recent advances in the kinetics of oxygen reduction. In *Electrocatalysis*; Lipkowski, J., Ross, P. N., Eds.; Wiley-VCH: New York, 1998; pp 197-242.

(19) Markovic, N. M.; Schmidt, T. J.; Stamenkovic, V.; Ross, P. N. *Fuel Cells* **2001**, *1*, 105.

(20) Wang, J. X.; Markovic, N. M.; Adzic, R. R. *Journal of Physical Chemistry B* **2004**, 4127.

(21) Itaya, K. *Prog. Surface Science* **1998**, *58*, 121.

(22) Lucas, C. A.; Markovic, N. M.; Ross, P. N. *Physical Review Letters* **1996**, *77*, 4922.

(23) Tidswell, I. M.; Markovic, N. M.; Ross, P. N. *Physical Review Letters* **1993**, *71*, 1601.

(24) Markovic, N. M.; Ross, P. N. *Surface Science Report* **2002**, *45*, 117.

(25) Mukerjee, S.; Srinivasan, S.; Soriaga, M. P. *Journal of Physical Chemistry* **1995**, *99*, 4577

(26) Yu, P.; Pemberton, M.; Plasse, P. *Journal of Power Source* **2004**, *144*, 11.

(27) Paulus, U. A.; Vokaun, A.; Scherer, G. G.; Schmidt, T. J.; Stamenkovic, V.; Radmilovic, V.; Markovic, N. M.; Ross, P. N. *Journal of Physical Chemistry B* **2002**, *106*, 4181.

(28) Paulus, U. A.; Vokaun, A.; Scherer, G. G.; Schmidt, T. J.; Stamenkovic, V.; Markovic, N. M.; Ross, P. N. *Electrochimie Acta* **2002**, *47*, 3787.

(29) Mukerjee, S.; Srinivasan, S. *J. Electroanalytical Chemistry.* **1993**, *357*, 201.

(30) Atrazhev, V.; Burlatsky, S. F.; Cipollini, N. E.; Condit, D. A.; Erikhman, N. *ECS Transactions* **2006**, *1*, 239.

(31) Crum, M.; Liu, W. *ECS Transactions* **2006**, *3*, 541.

(32) Liu, W.; Crum, M. *ECS Transactions* **2006**, *3*, 531.

(33) Lee, C.; Merida, W. *Journal of Power Sources* **2007**, *164*, 141.

(34) Borup, R. L.; Davey, J. R.; Garzon, F. H.; Wood, D. L.; Inbody, M. A. *Journal of Power Sources* **2006**, *163*, 76.

(35) Ferreira, P. J.; la O, G. J.; Shao-Horn, Y.; Morgan, D.; Makharia, R.; Kocha, S. S.; Gasteiger, H. A. *Journal of The Electrochemical Society* **2005**, *152*, A2256.

(36) Yu, J.; Matsuura, T.; Yoshikawa, Y.; Islam, M. N.; Hori, M. *Electrochemical and Solid-State Letters* **2005**, *8*, A156.

(37) Cleghorn, S. J. C.; Mayfield, D. K.; Moore, D. A.; Moore, J. C.; Rusch, G.; Sherman, T. W.; Sisofo, N. T.; Beuscher, U. *Journal of Power Sources* **2006**, *158*, 446.

(38) Liu, D.; Case, S. *Journal of Power Sources* **2006**, *162*, 521.

(39) Taniguchi, A.; Akita, T.; Yasuda, K.; Miyazaki, Y. *Journal of Power Sources* **2004**, *130*, 42.

(40) Knights, S. D.; Colbow, K. M.; St-Pierre, J.; Wilkinson, D. P. *Journal of Power Sources* **2004**, *127*, 127.

(41) Guilminot, E.; Corcella, A.; Charlot, F.; Maillard, F.; Chatenet, M. *Journal of the Electrochemical Society* **2007**, *154*, B96.

(42) Roh, W.; Cho, J.; Kim, H. *Journal of Applied Electrochemistry* **1996**, *26*, 623.

(43) Kim, K. T.; Kim, Y. G.; Chung, J. S. *Journal of the Electrochemical Society* **1995**, *142*, 1531.

(44) Honji, A.; Mori, T.; Tamura, K.; Hishinuma, Y. *Journal of the Electrochemical Society* **1988**, *135*, 355.

(45) Xie, J.; Wood, D. L., III; Wayne, D. M.; Zawodzinski, T. A.; Atanassov, P.; Borup, R. L. *Journal of the Electrochemical Society* **2005**, *152*, A104.

(46) Xie, J.; Wood, D. L.; Wayne, D. M.; Zawodzinski, T. A.; Atanassov, P.; Borup, R. L. *Journal of the Electrochemical Society* **2005**, *152*, A104.

(47) Yasuda, K.; Taniguchi, A.; Akita, T.; Ioroi, T.; Siroma, Z. *Journal of the Electrochemical Society* **2006**, *153*, A1599.

(48) Ferreira, P. J.; O, G. J. I.; Shao-Horn, Y.; Morgan, D.; Makharia, R.; Kocha, S.; Gasteiger, H. A. *Journal of the Electrochemical Society* **2005**, *152*, A2256.

(49) Colon-Mercado, H. R.; Popov, B. N. *Journal of Power Sources* **2005**, *155*, 253.

(50) Lukaszewski, M.; Czerwinski, A. *Journal of Electroanalytical Chemistry* **2006**, *589*, 38.

(51) Yu, P.; Pemberton, M.; Plasse, P. *Journal of Power Sources* **2005**, *144*, 11.

(52) Dam, V. A. T.; de Bruijn, F. A. *Journal of the Electrochemical Society* **2007**, *154*, B494.

(53) Wang, X.; Kumar, R.; Myers, D. J. *Electrochemical and Solid-State Letters* **2006**, *9*, A225.

(54) Aragane, J.; Urushibata, H.; Murahashi, T. *Journal of Applied Electrochemistry* **1996**, *26*, 147.

(55) Darling, R. M.; Meyers, J. P. *Journal of the Electrochemical Society* **2003**, *150*, A1523.

(56) Darling, R. M.; Meyers, J. P. *Proceedings - Electrochemical Society* **2005**, *2002-31*, 44.

(57) Wang, X. P.; Kumar, R.; Myers, D. J. *Electrochem. Sol. St. Lett.* **2006**, *9*, A225.

(58) Jerkiewicz, G.; Vatankhah, G.; Lessard, J.; Soriaga, M. P.; Park, Y.-S. *Electrochimica Acta* **2004**, *49*, 1451.

(59) Alsabet, M.; Grden, M.; Jerkiewicz, G. *Journal of Electroanalytical Chemistry* **2006**, *589*, 120.

(60) Nagy, Z.; You, H. *Electrochimica Acta* **2002**, *47*, 3037.

(61) McMillan, N.; Lele, T.; Snively, C.; Lauterbach, J. *Catalyst Today* **2005**, *105*, 244.

(62) Leisenberger, F. P.; Koller, G.; Sock, M.; Surnev, S.; Ramsey, M. G.; Netzer, F. P.; Klotzer, B.; Hayek, K. *Surface Science* **2000**, *445*, 380.

(63) Walker, A. V.; Klotzer, B.; King, D. A. *Journal of Chemical Physics* **2000**, *112*, 8631.

(64) Blume, R.; Niehus, H.; Conrad, H.; Bottcher, A. *Journal of Chemical Physics* **2004**, *120*, 3871.

(65) Blume, R.; Niehus, H.; Conrad, H.; Bottcher, A.; Aballe, L.; Gregoratti, L.; Barinov, A.; Kiskinova, M. *Journal of Physical Chemistry B* **2005**, *109*, 14052.

(66) Rose, M. K.; Borg, A.; Mitsui, T.; Ogletree, D. F.; Salmeron, M. *Journal of Chemical Physics* **2001**, *115*, 10927.

(67) Monine, M.; Pismen, L.; Bar, M.; Or-Guil, M. *Journal of Chemical Physics* **2002**, *117*, 4473.

(68) Xu, Y.; Greeley, J.; Mavrikakis, M. *Journal of American Chemical Society* **2005**, *127*, 12823.

(69) Rotermund, H. H.; Pollmann, M.; Kevrekidis, I. G. *Chaos* **2002**, *12*, 157.

(70) Over, H.; Seitsonen, A. P. *Science* **2002**, *297*, 2003.

(71) Savinova, D. V.; Molodkina, E. B.; Danilov, A. I.; Polukarov, Y. M. *Russian Journal of Electrochemistry* **2004**, *40*, 683.

(72) Savinova, D. V.; Molodkina, E. B.; Danilov, A. I.; Polukarov, Y. M. *Russian Journal of Electrochemisty* **2004**, *40*, 687.

(73) Nagy, Z.; You, H. *Electrochimica Acta* **2002**, *47*, 3037.

(74) Jerkiewicz, G.; Vatankhah, G.; Lessard, J.; Soriaga, M. P.; Park, Y.-S. *Electrochimica Acta* **2004**, *49*, 1451.

(75) Zhang, J.; Vukmirovic, M. B.; Xu, Y.; Mavrikakis, M.; Adzic, R. R. *Angewandte Chemie Int. Ed.* **2005**, *44*, 2132.

(76) Shao, M. H.; Sasaki, K.; Adzic, R. R. *Journal of American Chemical Socity* **2006**, *128*, 3526.

(77) Norskov, J. K.; Rossmeisl, J.; Logadottir, A.; Lindqvist, L.; Kitchin, J. R.; Bligaard, T.; Jonsson, H. *Journal of Physical Chemistry B* **2004**, *108*, 17886.

(78) Markovic, N. M.; Schmidt, T. J.; Stamenkovic, V.; Ross, P. N. *Fuel Cells* **2001**, *1*, 105.

(79) Hohenberg, P.; Kohn, W. *Physical Review B* **1964**, *136*, B864.

(80) Kohn, W.; Sham, L. J. *Physical Review* **1965**, *140*, A1133.

(81) Perdew, J. P.; Burke, K.; Wang, Y. *Physical Review B: Condensed Matter* **1996**, *54*, 16533.

(82) Perdew, J. P.; Chevary, J. A.; Vosko, S. H.; Jackson, K. A.; Pederson, M. R.; Singh, D. J.; Fiolhais, C. *Physical Review B* **1992**, *46*, 6671.

(83) Perdew, J. P.; Wang, Y. *Physical Review B* **1992**, *45*, 13244.

(84) Becke, A. D. *Physical Review A* **1988**, *38*, 3098.

(85) Lee, C.; Yang, W.; Parr, R. G. *Physical Review B* **1988**, *37*, 785.

(86) Perdew, J. P. *Physical Review B* **1986**, *33*, 8822.

(87) Becke, A. D. *Journal of Chemical Physics* **1996**, *104*, 1040.

(88) Becke, A. D. *Journal of Chemical Physics* **1997**, *107*, 8554.

(89) Schmider, H. L.; Becke, A. D. *Journal of Chemical Physics* **1998**, *108*, 9624.

(90) Perdew, J. P.; Burke, K.; Ernzerhof, M. *Physical Review Letters* **1996**, *77*, 3865.

(91) Perdew, J. P.; Burke, K.; Ernzerhof, M. *Physica Review Letters.* **1997**, *78*, 1396.

(92) Frisch, M. J.; Trucks, G. W.; Schlegel, H. B.; Scuseria, G. E.; Robb, M. A.; Cheeseman, J. R.; Montgomery, J. A.; Vreven, T.; Kudin, K. N.; Burant, J. C.; Millam, J. M.; Iyengar, S. S.; Tomasi, J.; Barone, V.; Mennucci, B.; Cossi, M.; Scalmani, G.; Rega, N.; Petersson, G. A.; Nakatsuji, H.; Hada, M.; Ehara, M.; Toyota, K.; Fukuda, R.; Hasegawa, J.; Ishida, M.; Nakajima, T.; Honda, Y.; Kitao, O.; Nakai, H.; Klene, M.; Li, X.; Knox, J. E.; Hratchian, H. P.; Cross, J. B.; Bakken, V.; Adamo, C.; Jaramillo, J.; Gomperts, R.; Stratmann, R. E.; Yazyev, O.; Austin, A. J.; Cammi, R.; Pomelli, C.; Ochterski, J. W.; Ayala, P. Y.; Morokuma, K.; Voth, G. A.; Salvador, P.; Dannenberg, J. J.; Zakrzewski, V. G.; Dapprich, S.; Daniels, A. D.; Strain, M. C.; Farkas, O.; Malick, D.

K.; Rabuck, A. D.; Raghavachari, K.; Foresman, J. B.; Ortiz, J. V.; Cui, Q.; Baboul, A. G.; Clifford, S.; Cioslowski, J.; Stefanov, B. B.; Liu, G.; Liashenko, A.; Piskorz, P.; Komaromi, I.; Martin, R. L.; Fox, D. J.; Keith, T.; Al-Laham, M. A.; Peng, C. Y.; Nanayakkara, A.; Challacombe, M.; Gill, P. M. W.; Johnson, B.; Chen, W.; Wong, M. W.; Gonzalez, C.; Pople, J. A. Gaussian03; Revision C.02 ed.; Gaussian, Inc.: Wallingford, CT, 2004.

(93) Becke, A. D. *Journal of Chemical Physics* **1993**, *98*, 5648.

(94) Wadt, W. R.; Hay, P. J. *Journal of Chemical Physics* **1985**, *82*, 284.

(95) Balbuena, P. B.; Altomare, D.; Vadlamani, N.; Bingi, S.; Agapito, L. A.; Seminario, J. M. *Journal of Physical Chemistry A* **2004**, *108*, 6378.

(96) Jacob, T.; Muller, R. P.; W. A. Goddard, I. *Journal of Physical Chemistry B* **2003**, *107*, 9465.

(97) Li, T.; Balbuena, P. B. *Journal of Physical Chemistry. B* **2001**, *105*, 9943.

(98) Wang, Y.; Balbuena, P. B. *Journal of Physical Chemistry. B* **2005**, *109*, 18902.

(99) Kresse, G.; Furthmuller, *Physical Review B* **1996**, *54*, 11169.

(100) Kresse, G.; Furthmuller, *Journal* of *Comput. Mater. Sci.* **1996**, *6*, 15.

(101) Blochl, P. E. *Physical Review B* **1994**, *50*, 17953.

(102) Kresse, G.; Joubert, D. *Physical Review B* **1999**, *59*, 1758.

(103) Monkhorst, H. J.; Pack, J. D. *Physical Review B* **1976**, *13*, 5188.

(104) Branger, V.; Pelosin, V.; Badawi, K. F.; Goudeau, P. *Thin Solid Films* **1996**, *275*, 22.

(105) Henkelman, G.; Jonsson, H. *Journal of Chemical Physics* **2000**, *113*, 9978.

(106) Henkelman, G.; Uberuaga, B. P.; Jonsson, H. *Journal of Chemical Physics* **2000**, *113*, 9901.

(107) Jonsson, H.; Mills, G.; Jacobsen, K. W. Nudged Elastic Band Method for Finding Minimum Energy Paths of Transitions. In *Classical and Quantum Dynamics in*

Condensed Phase Simulation; Berne, B. J., Cicotti, G., Coker, D. F., Eds.; World Scientific: New York,1998; pp 385.

(108) Tawa, G. J.; Topol, I. A.; Burt, S. K.; Caldwell, R. A.; Rashin, A. A. *Journal of Chemical Physics* **1998**, *109*, 4852.

(109) Cotton, A. F.; Wilinson, G.; Murillo, C. A.; Bochmann, M. *Advanced Inorganic Chemistry*, 6th ed.; Wiley: New York, 1999.

(110) Yeo, Y. T.; Vattuone, L.; King, D. A. *Journal of Chemical Physics* **1997**, *106*, 392.

(111) Gambardella, P.; Sljivancanin, Z.; Hammer, B.; Blanc, M.; Kuhnke, K.; Kern, K. *Physical Review Letters* **2001**, *87*, 056103.

(112) Parker, D. H.; Bartram, M. E.; Koel, B. E. *Surface Science.* **1989**, *217*, 489.

(113) Lee, W. H.; Vanloon, K. R.; Petrova, V.; Woodhouse, J. B.; Loxton, C. M.; Masel, R. I. *Journal of Catalysis* **1990**, *126*, 658.

(114) Ganduglia-Pirovano, M. V.; Reuter, K.; Scheffler, M. *Physical Review B* **2002**, *65*, 245426.

(115) Gu, Z.; Balbuena, P. B. *Journal of Physical Chemistry C* **2007**.

(116) Bogicevic, A.; Stromquist, J.; Lundqvist, B. I. *Physical Review B* **1998**, *57*, R4289

(117) Odelius, M.; Cavalleri, M.; Nilsson, A.; Pettersson, L. G. M. *Physical Review B* **2006**, *73*, 024205.

(118) Gu, Z.; Balbuena, P. B. *Journal of Physical Chemistry C* **2007**, *111*, 9877.

(119) Sanville, E.; Kenny, S. D.; Smith, R.; Henkelman, G. *Journal of Computational Chemistry* **2007**, *28*, 899.

(120) Kootte, A.; Haas, C.; de Groot, R. A. *Journal of Physics: Condense Matter* **1991**, *3*, 1133.

(121) Ioroi, T.; Yasuda, K. *Journal of the Electrochemical Society* **2005**, *152*, A1917.

(122) Toda, T.; Igarashi, H.; Uchida, H.; Watanabe, M. *Journal of the Electrochemical Society* **1999**, *146*, 3750.

(123) Igarashi, H.; Fujino, T.; Zhu, Y.; Uchida, H.; Watanabe, M. *Physical Chemistry Chemical Physics* **2001**, *3*, 306.

(124) Wan, L.-J.; Moriyama, T.; Ito, M.; Uchida, H.; Watanabe, M. *Chemical Communications (Cambridge, United Kingdom)* **2002**, 58.

(125) Stamenkovic, V.; Schmidt, T. J.; Ross, P. N.; Markovic, N. M. *Journal of Physical Chemistry B* **2002**, *106*, 11970.

(126) Ruban, A. V.; Skriver, H. L.; Norskov, J. K. *Physical Review B: Condensed Matter and Materials Physics* **1999**, *59*, 15990.

(127) Erlebacher, J.; Aziz, M. J.; Karma, A.; Dimitrov, N.; Sleradzki, K. *Nature (London, United Kingdom)* **2001**, *410*, 450.

(128) Newman, R. C.; Sieradzki, K. *Science (Washington, DC, United States)* **1994**, *263*, 1708.

APPENDIX A

Supplemental data for Chapter III are listed as following:

Table A-1: Gibbs free energies (Δ G, in eV) calculated with B3LYP/Lan2dz & 6-311++g(d,p) of dissolution reactions 1 to 5 of Pt, Ir, Pd, Rh, Ni, Co, modeling the hydrated cation as $M^{2+}(H_2O)_6$.

	R. 1	R. 2	R. 3	R. 4	R. 5
Pt	-7.12	-4.88	-5.25	-21.44	-13.87
Ir	-7.17	-4.81	-5.28	-20.64	-13.88
Pd	-6.87	-6.34	-6.05	-22.50	-14.03
Rh	-7.79	-5.79	-6.98	-22.03	-14.39
Ni	-9.52	-8.09	-11.22	-24.41	-15.92
Co	-9.76	-8.10	-11.66	-24.53	-15.95

Table A-2: Gibbs free energies (Δ G, in eV) calculated with B3LYP/Lan2dz & 6-311++g(d,p) of dissolution reactions 1 to 5 of Pt, Ir, Pd, Rh, Ni, Co, modeling the hydrated cation as $M^{2+}(H_2O)_4$.

	R. 1	R. 2	R. 3	R. 4	R. 5
Pt	-6.26	-4.03	-3.54	-20.59	-13.01
Ir	-6.42	-4.05	-3.77	-19.89	-13.12
Pd	-5.23	-4.71	-2.78	-20.86	-12.39
Rh	-6.26	-4.26	-3.92	-20.50	-12.86
Ni	-6.93	-5.50	-6.04	-21.82	-13.33
Co	-7.96	-6.31	-8.07	-22.73	-14.16

Table A-3: Gibbs free energies (Δ G, in eV) calculated with B3LYP/Lan2dz & 6-311++g(d,p) of dissolution reactions 1 to 5 of PtPt, IrIr, PdPd, RhRh, NiNi, CoCo, modeling the hydrated cation as $M^{2+}(H_2O)_6$.

	R. 1	R. 2	R. 3	R. 4	R. 5
PtPt	-5.00	-3.68	-1.66	-20.17	-12.04
IrIr	-4.43	-1.69	0.10	-18.11	-10.65
PdPd	-6.60	-6.37	-5.41	-22.52	-14.16
RhRh	-6.66	-4.90	-4.74	-21.03	-13.49
NiNi	-7.98	-6.76	-8.20	-22.73	-14.52
CoCo	-8.32	-5.16	-8.74	-21.53	-13.07

Table A-4: Gibbs free energies (Δ G, in eV) calculated with B3LYP/Lan2dz & 6-311++g(d,p) of dissolution reactions 1 to 5 of PtPt, IrIr, PdPd, RhRh, NiNi, CoCo, modeling the hydrated cation as $M^{2+}(H_2O)_4$.

	R. 1	R. 2	R. 3	R. 4	R. 5
PtPt	-4.15	-2.83	0.05	-19.32	-11.18
IrIr	-3.68	-0.93	1.61	-17.36	-9.90
PdPd	-4.87	-4.64	-1.94	-20.78	-12.43
RhRh	-5.13	-3.37	-1.68	-19.50	-11.96
NiNi	-5.39	-4.17	-3.02	-20.14	-11.93
CoCo	-6.52	-3.36	-5.14	-19.74	-11.27

Table A-5: Gibbs free energies (Δ G, in eV) calculated with B3LYP/Lan2dz & 6-311++g(d,p) of dissolution reactions 1 to 5 of PtPt, PtIr, PtPd, PtRh, PtNi, PtCo, Pt is the adsorption site, modeling the hydrated cation as $Pt^{2+}(H_2O)_6$.

	R. 1	R. 2	R. 3	R. 4	R. 5
PtPt	-5.00	-3.68	-1.66	-20.17	-12.04
PtIr	-5.54	-3.18	-1.92	-20.67	-12.33
PtPd	-5.70	-4.26	-2.76	-20.57	-12.90
PtRh	-5.79	-4.33	-3.05	-21.31	12.86
PtNi	-4.90	-3.76	-1.68	-20.02	-11.89
PtCo	-7.34	-4.01	-3.93	-22.42	-14.76

Table A-6: Gibbs free energies (Δ G, in eV) calculated with B3LYP/Lan2dz & 6-311++g(d,p) of dissolution reactions 1 to 5 of PtPt, PtIr, PtPd, PtRh, PtNi, PtCo, Pt is the adsorption site, modeling the hydrated cation as $Pt^{2+}(H_2O)_4$.

	R. 1	R. 2	R. 3	R. 4	R. 5
PtPt	-4.15	-2.83	0.05	-19.32	-11.18
PtIr	-4.68	-2.32	-0.21	-19.82	-11.47
PtPd	-4.85	-3.40	-1.04	-19.72	-12.04
PtRh	-4.93	-3.47	-1.33	-20.46	-12.00
PtNi	-4.04	-2.90	0.04	-19.16	-11.03
PtCo	-6.48	-3.16	-2.22	-21.57	-13.91

Table A-7: Gibbs free energies (Δ G, in eV) calculated with B3LYP/Lan2dz & 6-311++g(d,p) of dissolution reactions 1 to 5 of PtPt, PtIr, PtPd, PtRh, PtNi, PtCo, second metal M is the adsorption site, modeling the hydrated cation as $M^{2+}(H_2O)_6$.

	R. 1	R. 2	R. 3	R. 4	R. 5
PtPt	-5.00	-3.68	-1.66	-20.17	-12.04
PtIr	-4.84	-2.08	-0.63	-18.56	-11.13
PtPd	-5.94	-5.82	-4.06	-22.03	-13.63
PtRh	-6.20	-4.69	-3.86	-20.98	-13.24
PtNi	-7.30	-6.12	-7.07	-22.41	-13.64
PtCo	-7.30	-5.67	-6.88	-22.05	-13.40

Table A-8: Gibbs free energies (Δ G, in eV) calculated with B3LYP/Lan2dz & 6-311++g(d,p) of dissolution reactions 1 to 5 of PtPt, PtIr, PtPd, PtRh, PtNi, PtCo, second metal M is the adsorption site, modeling the hydrated cation as $M^{2+}(H_2O)_4$.

	R. 1	R. 2	R. 3	R. 4	R. 5
PtPt	-4.15	-2.83	0.05	-19.32	-11.18
PtIr	-4.09	-1.32	0.88	-17.80	-10.37
PtPd	-4.20	-4.08	-0.59	-20.30	-11.90
PtRh	-4.67	-3.16	-0.80	-19.45	-11.71
PtNi	-4.70	-3.53	-1.89	-19.82	-11.05
PtCo	-5.50	-3.88	-3.29	-20.25	-11.60

APPENDIX B

Supplemental data for Chapter VI are listed as following:

Table B-1: The energy barriers (eV) and reverse energy (eV) barriers for atomic oxygen diffusion on PtX surface and absorption into subsurfaces.

	PtCo	PtNi	PtRu	PtRh	PtPd*	PtIr	Pure Pt
Surface diffusion from fcc-2 to hcp-2							
Energy barrier	0.25	0.39	0.30	0.52	0.45	0.43	0.60
Reverse barrier	0.21	0.38	0.20	0.28	0.08	0.19	0.20
Absorption from hcp-2 to tetra-2							
Energy barrier	1.40	1.36	2.12	2.58	2.07	2.88	2.22
Reverse barrier	0.01	0.16	0.00	0.64	0.34	0.66	0.70

* fcc-1 to hcp-1 for surface diffusion and hcp-1 to tetra-1 for absorption.

Table B-2: Pt-X bond distance (R_{PtX}/ Å) and X-X bond distance (R_{XX}/ Å) at the hcp site in the top layer which coordinates with absorbed O; Pt-O bond dostance (R_{PtO}/ Å) and X-O bond distance (R_{XO}/ Å) between O and Pt, and X atoms in the top layer; the vertical distance between top and second layer ($D_{1\sim2}$/ Å), maximum vertical distance of atoms in top layer (D1~1/ Å), vertical distance ($D_{1\sim O}$) of absorbed O to top layer for atomic oxygen adsorbed on hcp site, at the transition state (TS) for migration to the subsurface, and in subsurface tetrahedral site with total coverage of 0.25 ML.

		Pt-Co	Pt-Ni	Pt-Ru	Pt-Rh	Pt-Pd*	Pt-Ir
hcp-2	R_{PtX}	2.754	2.744	2.873	2.841	2.845	2.909
	R_{XX}	2.827	2.706	2.892	2.820	2.904	2.894
	R_{PtO}	2.072	2.033	2.105	2.048	2.008	2.102
	R_{XO}	1.876	1.859	1.984	1.997	2.144	2.009
	$D_{1\sim2}$	2.192	2.250	2.282	2.315	2.333	2.339
	$D_{1\sim1}$	0.100	0.118	0.149	0.122	0.158	0.218
TS	R_{PtX}	3.130	3.089	3.312	3.182	3.285	3.211
	R_{XX}	3.128	3.126	3.061	3.182	3.110	3.194
	R_{PtO}	1.972	1.941	2.012	1.871	1.870	1.887

	R_{XO}	1.749	1.725	1.948	1.830	1.887	1.849
	$D_{1\sim2}$	2.285	2.280	2.504	2.442	2.540	2.500
	$D_{1\sim1}$	0.503	0.379	0.913	0.360	0.684	0.405
Tetra-2	R_{PtX}	3.068	3.019	3.164	3.069	3.085	3.105
	R_{XX}	3.101	3.061	3.110	3.071	3.117	3.108
	R_{PtO}	2.005	1.990	2.019	1.991	1.961	2.014
	R_{XO}	1.784	1.774	1.962	1.928	1.968	1.956
	$D_{1\sim2}$	2.339	2.364	2.539	2.543	2.610	2.588
	$D_{1\sim1}$	0.397	0.214	0.700	0.385	0.319	0.440
	$^{**}D_{1\sim O}$	-0.530	-0.559	-0.710	-0.751	-0.756	-0.776
ΔR_{PtX}/ hcp-2→TS		0.376	0.345	0.439	0.341	0.440	0.302
ΔR_{XX}/ hcp-2→TS		0.301	0.420	0.169	0.362	0.206	0.300
$\Delta D_{1\sim2}$/ hcp-2→TS		0.093	0.030	0.222	0.127	0.207	0.161
$\Delta D_{1\sim1}$/ hcp-2→TS		0.403	0.261	0.764	0.238	0.508	0.187
ΔR_{PtX}/ tetra-2→TS		0.062	0.070	0.148	0.113	0.200	0.106
ΔR_{XX}/ tetra-2→TS		0.027	0.065	-0.049	0.111	-0.007	0.086
$\Delta D_{1\sim2}$/ tetra-2→TS		-0.054	-0.084	-0.035	-0.100	-0.070	-0.088
$\Delta D_{1\sim1}$/ tetra-2→TS		0.106	0.165	0.213	-0.015	0.299	-0.035

* fcc-1 to hcp-1 for surface diffusion and hcp-1 to tetra-1 for absorption.
** negative means below top layer.

Table B-3: DFT calculated Pt-Pt bond length (R_{PtPt}) at the hcp site in the top layer which coordinates with absorbed O, the average vertical distance ($D_{1\sim2}$) between top and second Pt layer, the vertical distance ($D_{top\ layer}$)of Pt atoms in top layer, vertical distance ($D_{1\sim O}$) of absorbed O to Pt top layer, for atomic oxygen adsorbed on hcp site, at the transition state (TS) for migration to the subsurface, and in subsurface tetrahedral site with total coverage of 0.25 ML.

		Pure Pt	Pt skin/ Pt_3Ru	Pt skin/ Pt_2IrRu
hcp	R_{PtPt}	2.875	2.846	2.803
	$D_{1\sim2}$	2.410	2.342	2.332
	$D_{top\ layer}$		0.088	0.187
TS	R_{PtPt}	3.208	3.205	3.180
	$D_{1\sim2}$	2.611	2.496	2.516
	$D_{top\ layer}$		0.120	0.266
tetra	R_{PtPt}	3.117	3.099	3.062
	$D_{1\sim2}$	2.619	2.598	2.622
	$D_{top\ layer}$		0.242	0.284
	$D_{1\sim O}$		0.784	0.799
R_{PtPt} change/ from hcp to TS		0.333	0.359	0.377
$D_{1\sim2}$ change/ from hcp to TS		0.201	0.154	0.184
R_{PtPt} change/ from tetra to TS		0.091	0.106	0.118
$D_{1\sim2}$ change/ from tetra to TS		-0.008	-0.102	-0.108

Table B-4: Change of Pt-Pt bond length (R_{PtPt}/ Å) at the hcp site in the top layer which coordinates with absorbed O, the change of average vertical distance between top and second layer ($D_{1\sim2}$/ Å), and atomic oxygen charge change(ΔC) from hcp sites to transition states (TS) for oxygen migration to the subsurface tetrahedral site with total coverage of 0.25 ML.

0.25 ML coverage	Pure Pt	Pt skin/Pt_3Ru	Pt skin/Pt_2IrRu
R_{PtPt} change/ hcp to TS	0.333	0.359	0.377
$D_{1\sim2}$ change/ hcp to TS	0.201	0.154	0.184
R_{PtPt} change/ tetra to TS	0.091	0.106	0.118
$D_{1\sim2}$ change/ tetra to TS	-0.008	-0.102	-0.108
$\Delta C_{hcp\text{-}TS}$	-0.3326	-0.3613	-0.3486
$\Delta C_{tetra\text{-}TS}$	-0.1034	-0.1092	-0.1010

VITA

Name: Zhihui Gu

Address: Department of Chemical Engineering, TAMU 3122
Texas A&M University
College Station, Texas, 77843

Email: zhihui.gu@chemail.tamu.edu

Education: B.S. Chemical Engineering, Tianjin University, China, 1993
Ph.D. Chemical Engineering, Texas A&M University, 2007

Professional experience:

Graduate Research Assistant, Chemical Engineering Department at Texas A&M University, College Station, Texas, 2004 ~ 2007

Graduate Research Assistant, Chemical Engineering Department at University of South Carolina, Columbia, South Carolina, 2002 ~ 2004

Chemical Research Engineer, Research Institute of SINOPEC Yangzi Petrochemical Company, China, 1993 ~ 2002

Publication: Gu, Zhihui; Balbuena, Perla B. *Chemical environment effects on atomic oxygen absorption into Pt(111) subsurface of cathode catalyst*. *Journal of Physical Chemistry C*, Accepted.

Gu, Zhihui; Balbuena, Perla B. *Absorption of atomic oxygen into subsurfaces of Pt(100) and Pt(111): Density functional theory study*. *Journal of Physical Chemistry C* **2007**, 111, 9877.

Gu, Zhihui; Balbuena, Perla B. *Dissolution of Oxygen Reduction Electrocatalysts in an Acidic Environment: Density Functional Theory Study*. *Journal of Physical Chemistry A* **2006**, 110, 9783.

Gu, Zhihui; Wang, Yixuan; Balbuena, Perla B. *Does the Decomposition of Peroxydicarbonates and Diacyl Peroxides Proceed in a Stepwise or Concerted Pathway*? *Journal of Physical Chemistry A* **2006,** 110, 2448.

Gu, Zhihui; Balbuena, Perla B. *Structural characterization of Pt nanoclusters deposited on graphite: Effects of substrate and surrounding medium*. *Catalysis Today* **2005**, 105, 152.

Gu, Zhihui; Sandi, Giselle; Balbuena, Perla B. *Molecular dynamics characterization of polymer confinement in nanocomposite catalytic membranes*. *Journal of New Materials for Electrochemical Systems* **2004**, 7, 7.